Front page

Exam information
NFYA09004E - Nanoscience Thesis 60 ECTS, Niels Bohr Institute - Contract:134131 (Aliki Gerakianaki)

Handed in by
Aliki Gerakianaki
wgm492@alumni.ku.dk

Exam administrators
Eksamensteam, tel 35 33 64 57
eksamen@science.ku.dk

Assessors
Heloisa Nunes Bordallo
Examiner
bordallo@nbi.ku.dk
+4535321215

Kristine Niss
Co-examiner
kniss@ruc.dk

Hand-in information

Title: Mechanisms Behind Induced Polarization Effects in Water and Brines Confined in Oriented Clay Mineral Films
Title, english: Mechanisms Behind Induced Polarization Effects in Water and Brines Confined in Oriented Clay Mineral Films
The sworn statement: Yes
Does the hand-in contain confidential material: No

UNIVERSITY OF COPENHAGEN

MSc in Nanoscience

Mechanisms Behind Induced Polarization Effects in Water and Brines Confined in Oriented Clay Mineral Films

Aliki Gerakianaki

Supervised by Heloisa N. Bordallo and Will P. Gates

May 2023

Aliki Gerakianaki
Mechanisms Behind Induced Polarization Effects in Water and Brines Confined in Oriented Clay Mineral Films
MSc in Nanoscience, May 2023
Supervisors: Heloisa N. Bordallo and Will P. Gates

University of Copenhagen
Niels Bohr Institute
Masters Degree in Nanoscience
Universitetsparken 5
2100 Copenhagen Ø

Abstract

Clay minerals have garnered significant attention as hydraulic barriers in landfills due to their exceptional ability to mitigate contaminant transport. The study of water dynamics in clays is crucial for improving the design and performance of engineered barriers. The primary objective of this masters' research project is to investigate the diffusion behavior of water, as well as water with salt concentrations of NaCl and $CaCl_2$, confined in clay mineral oriented films. Furthermore, it is to analyze how applied electric field stimulation affects the diffusion processes. To achieve this objective, samples of hydrated montmorillonite, which is a specific type of smectite clay mineral, with varying salt concentrations were analyzed using quasi elastic neutron scattering (QENS) at the time-of-flight spectrometer AMATERAS (J-PARC, Japan). The analysis of the samples revealed that the time window covered by the instrument resolution and the dynamical range covered by the spectrometer allowed for the observation of translational motions of more than one water molecule populations. More specifically, despite the lack of discernible effects of electrical field or salt inclusion on the diffusive processes observed in the spectra analysis, the susceptibility plots revealed distinct and more detailed results, contradicting what was considered to be true from the initial data analysis. To fully assess the smectite data, previous samples of bulk-water were studied using QENS at the backscattering spectrometer IRIS (ISIS, UK) to comprehend and confirm the correlation between the use of different approaches, such as the Singwi-Sjölander and minimalistic models.

Contents

1 Introduction

Comprehending the characteristics and conduct of water in soils is vital for a variety of fields, such as agriculture, ecology, hydrology and environmental science. Moreover, understanding the movement of water molecules within strong hydrogen-bonded environments can also have implication in fields such as chemistry and materials science. A significant challenge in recent years has been to unravel the mechanism by which water molecules, despite each being part of a three-dimensional network of strong hydrogen bonds that already exist at room temperature [1], move on a picosecond time scale and nanometer length scale. Neutron scattering experiments, particularly quasi elastic neutron scattering (QENS), offer insights into the dynamics of various water populations confined within interlayer clay minerals across a wide range of length scales [2]. Depending on the instrument's resolution and energy range coverage, we can gather information on the diffusion, vibration and rotation of water molecules.

Several studies involving neutron scattering and molecular dynamics have significantly advanced our understanding of the behavior of water molecules confined in clay minerals. The work of Porion et al. [2] highlights that a combination of experimental techniques, such as QENS, inelastic neutron scattering (INS) and molecular dynamics (MD), can be used to investigate the dynamic properties of water molecules and cations confined in clay minerals over a wide range of characteristic times and diffusion lengths. In this direction, Gates et al. [3] provided a clear description of the various water populations present in hydrated clays and the importance of the interlayer cations that significantly influence the dynamics and diffusivity of the water molecules within the interlayer space. Upon hydration, smectites tend to swell due to interactions between water and clay, resulting in volume changes. Interlayer cations primarily facilitate water uptake, and the type and charge of the cations can affect the interlayer surface. In addition to the structural water (1) which remains unaffected by hydration, four main water populations can be found in the interlayer: (2) interlayer water tightly bound to the cations (cation-

coordinated), (3) tightly H-bonded interlayer water that does not directly interact with the cations, (4) water weakly bonded to the interlayer surface and (5) intraparticle water. Research suggests that intraparticle water diffuses faster than the H-bonded and interlayer water, as the latter tends to remain within the interlayer [3]. Nevertheless, the cations present in the system are the primary influencers of the dynamics [4].

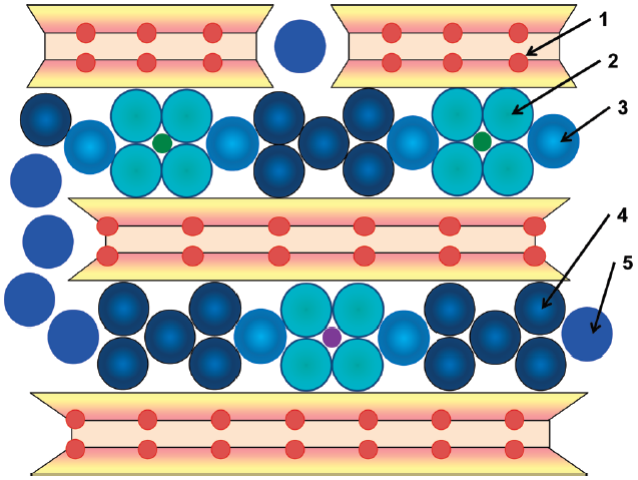

Figure 1.1: Water Populations found in a hydrated smectite: (1) structural water, (2) interlayer cation-coordinated water, (3) tightly H-bonded interlayer water, (4) weakly bonded to the interlayer surface water and (5) interparticle water. Each water population diffuses in different rates with (2) and (3) diffusing slower than (5) that behaves more like bulk water (figure obtained from [3]).

The presence of exchangeable cations such as Na^{+} and Ca^{2+} in the interlayers of clay minerals has been proven to have a significant role in the dynamics of confined water. These cations have the ability to attract water molecules and form hydration shells, which can greatly affect the physical and chemical properties of water and its behavior when confined in smectite nanopores. The presence of these cations also plays a critical role in the reabsorption of water into the interlayer pores of clays and can strongly impact the H-bondings within the system [5]. Ignazzi et al. [6] investigated the effects of an applied electric field on water molecules confined in a clay mineral, and it was found that cationic water can become highly distorted and polarized under an applied voltage.

Comprehending the alterations in water mobility under varying conditions holds paramount importance across multiple areas of study. The combined

interaction of electrical field and salinity on confined water in clay minerals is a topic of interest as it can have significant implications for environmental remediation, such as the stability of clay dams that hold tailings in place (red mud incident in Hungary 2010 figure 1.2 [7]). By studying the properties of confined water in clay minerals under electrical field stimulation and different salinity concentrations, researchers can gain a better understanding of how these factors affect water mobility, density, viscosity and diffusion coefficient.

Figure 1.2: Red Mud incident in Hungary (2010). The mud primarily contained iron (III) and aluminium oxides and was highly caustic, leading to several injuries, as well as the death of ten people [7].

This information can be used to develop better strategies for managing and conserving water resources, as well as for improving soil stability and plant nutrition. In the previous case, we can gain insight into how to effectively and safely remove water from clay dams (i.e. through electrolysis). This knowledge can also be applied in colder regions where thawing intervals have become longer due to global warming and where infrastructure is required to manage waste. Overall, the results of this study can be used to help mitigate potential hazards and promote sustainable practices and potentially contribute to a better understanding of how water behaves in natural systems and how it can be manipulated for various applications.

QENS is used to explore the displacements of atoms in a length scale of

a nanometer and time scales that reach that of a picosecond and for the purpose of this study was used in both bulk and confined water in clay minerals. In a hydrated sample, like the ones treated in this work, the incoherent scattering from the H-atoms is dominant, so that in all measured parameters the assumption is made that in QENS spectra only the incoherent scattering is measured and the coherent contributes only to the background, meaning that QENS explores particularly the diffusion motions of the individual hydrogen atoms. In a neutron scattering experiment, the wave-particle duality of the neutrons should be considered, as the incoming neutron interacts with the sample, resulting in a change of energy and orientation [5]. The quantity that is measured is the dynamic structure factor S(Q,ω) and gives insight into the various types of motions, rotations, translations and vibrations of the water molecules. The quasi-elastic response of the dynamic structure factor is the area of interest in this study, as it pertains to small energy exchanges.

For this work, QENS experiments on bulk water were conducted in the backscattering IRIS spectrometer in the UK by Dr. Mark T.F. Telling, while the experiments on the oriented films was done at the time-of-flight AMATERAS spectrometer installed at the J-Park Material and Life Science Facility in Japan by other members of the X-ray and neutron scattering group of the Niels Bohr Insitute as part of a long term proposal. Bulk-water data were analyzed using the Singwi-Sjölander model available in the Mantid software [8], which describes discrete jumps of the molecules from one point to another and a python script describing the minimalistic model [9], in which the interpretation of the data does not rely on fitting functions to capture the dynamics of the system. The analysis showed, as expected, that for bulk-water at room temperature, the different approaches used, led to results for the diffusion coefficient that are in good agreement with the so far reported bibliography, D_t=2.3 $10^{-9} m^2$/s [10, 11, 12, 13, 14]. While the analysis of these data has previously been done by Martin H. Petersen at room temperature, this current work was focused on the temperature dependence, as well as on reproducing the results with the Mantid software, which had not been done before.

The data of the clay mineral oriented films were fitted using the Dave Software [15] and fitted with both the Singwi-Sjölander and Chudley-Elliot model. The last one represents also descrete jumps from one point to another, but in this case the molecule jumps to another site that is seperated from the first one. From the analysis, it was found that in samples with different salt concentra-

tions the diffusion rates were actually affected, as well as when electric field was applied.

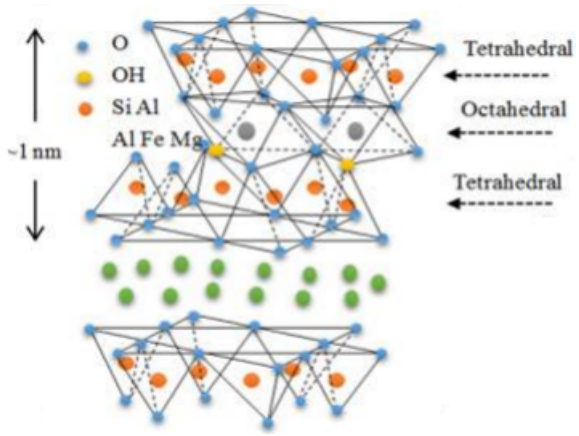

Figure 1.3: Basic Structure of smectites: Octahedral aluminum sheets (gray atoms) are bound by two tetrahedral silica sheets (orange atoms). The interlayer region can be occupied by exchangeable cations (green atoms). In this study, both Na^{+} and Ca^{2+} are used as cations for Mt (figure obtained from [16]).

Regarding confined water in clay minerals the sample used was **montmorillonite** (Mt) and belongs to the most commonly known dioctahedral smectites. The structure is mainly characterized by alumino-silicate layers (including oxygen and hydrogen); alumina octahedral sheets packed in between silica tetrahedral sheets [4]. In the interlayer region there can be exchangeable cations (i.e. Na^{+} or Ca^{2+}) as seen in figure 1.3. The Si in the tetrahedral sheets and the Al in the octahedral sheets can both be partially replaced by other atoms of similar size through isomorphous substitution. Common replacements for the tetrahedral Si^{4+} are Al^{3+} or Fe^{3+} and for the octahedral Al^{3+} are Mg^{2+} and $Fe^{2+,3+}$. Deviations from the ideal composition of montmorillonite cause differences in the electrical layer charge on the clay mineral. As indicated above the common replacements may be of lower valency than the ideal components resulting in a negative charge within the layer.

In the present work we begin in Chapter 2 with an overview of the basic concepts regarding the techniques used in the different studies, mainly focusing in neutron scattering and diffusion models.

Chapter 3 is dedicated to the materials used in the experiments and the approaching methods used for the analysis, while Chapter 4 is dedicated to

the results of the experiments and analysis done in confined water in Mt.

Finally, Chapter 5 is the summary of the main results of each experiment and analysis and presents perspectives for future work to be carried out.

Basic Theory

2

2.1 Basic Neutron Scattering Theory

Neutrons are non-charged particles that penetrate deeply into matter, allowing the study of the structure and the dynamics of materials, since they interact with the nucleus of an atom rather than the electronic cloud as X-rays do. In a neutron scattering experiment, the wave-particle duality should be considered, which indicates that neutrons are seen as particles when they are created, as interfering waves when they interact with matter and get scattered and again as particles when detected [5, 17].

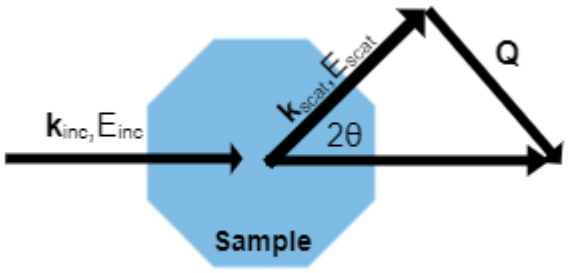

Figure 2.1: The scattering phenomenon: A neutron with an incident wave vector k_{inc} and energy E_{inc} interacts with the sample resulting in a change of energy E_{scat} and orientation k_{scat} into a diffusion angle of 2θ.

The diffusion angle, 2θ, is defined as the angle between the wave vectors $\mathbf{k}_{inc} = \frac{m_n \mathbf{v}_{inc}}{\hbar}$ and $\mathbf{k}_{scat} = \frac{m_n \mathbf{v}_{scat}}{\hbar}$, where m_n is the neutron mass, $\mathbf{v}_{inc}$ and $\mathbf{v}_{scat}$ are the incoming and scattered velocity respectively and $\hbar$ is Planck's constant. The momentum and energy conservation rules lead to:

$$\mathbf{Q} = |\mathbf{k}_{inc}| - |\mathbf{k}_{scat}| \tag{2.1}$$

and

$$\hbar\omega = E_{scat} - E_{inc} = \hbar(\omega_{scat} - \omega_{inc}) = \frac{\hbar^2({\omega_{scat}}^2 - \omega_{inc})^2}{2m_n} \tag{2.2}$$

where **Q** is the scattering vector measured in Å^{-1} and denotes the momentum transfer and $\hbar\omega$ is the energy transfer measured in meV. Molecular motions, such as vibration (10^{-14} to 10^{-15} s), diffusion (10^{-9} to 10^{-10} s) and rotation (10^{-11} to 10^{-12} s) are of similar order to these energy scales [5]. In the case of inelastic scattering, where $\hbar\omega \neq 0$, there will be energy exchange between neutrons and the sample leading to the scattering vector being a function of the energy ω, the wavelength λ and 2θ. In the case of elastic scattering, where $\hbar\omega = 0$, there will be no energy exchange and the scattering vector will be described by: $|\mathbf{Q}| = \frac{4\pi}{\lambda} sin(2\theta)$ with $\lambda = \lambda_{inc} = \lambda_{scat}$.

A neutron beam is defined by its flux Ψ, i.e. the number of neutrons crossing a unit area. The neutron scattering cross-section (σ) is by definition the number of neutrons scattered per second divided by the flux. In a neutron scattering experiment the quantity measured is the differential scattering cross-section $\frac{d^2\sigma}{d\Omega d\omega}$ and is the number of neutrons scattered over a solid angle dΩ and by energy transfer dω. If there is a system with more than one nuclei, the average differential cross-section can be calculated using Fermi's golden rule and the Fermi pseudopotential:

$$(\frac{d^2\sigma}{d\Omega d\omega}) = \frac{k_{scat}}{k_{inc}} \frac{1}{2\pi} \sum_{i,j} \langle n_i|b_i b_j|n_f\rangle \int_{-\infty}^{\infty} dt \left\langle n_i|e^{-i\mathbf{Q}\mathbf{r}_i(0)} e^{i\mathbf{Q}\mathbf{r}_j(t)}|n_k\right\rangle e^{-i\omega t} \tag{2.3}$$

where $\mathbf{r}(t)$ is the position operator, b is the scattering length describing the interactions between the neutrons and the nucleus and $|$ n $>$ refers to the energy state, where the indices represent the i and j nucleus. This equation is known as the master equation for scattering of unpolarized netrons, where spin-states are omitted [18].

2.1.1 Coherent and Incoherent Scattering

We can re-write equation 2.3 by separating into two parts, one describing correlation between N different scatters (i≠ j) and another one describing the self-correlation (i=j) between identical scatters [19]:

$$\begin{aligned}(\frac{d^2\sigma}{d\Omega d\omega}) = \frac{k_{scat}}{k_{inc}}\frac{1}{2\pi}\sum_{i\neq j}\langle b\rangle^2\int_{-\infty}^{\infty}dt\left\langle e^{-i\mathbf{Q}\mathbf{r}_i(0)}e^{i\mathbf{Q}\mathbf{r}_j(t)}\right\rangle e^{-i\omega t} \\ +\frac{k_{scat}}{k_{inc}}\frac{1}{2\pi}\sum_{i=j}\langle b\rangle^2\int_{-\infty}^{\infty}dt\left\langle e^{-i\mathbf{Q}\mathbf{r}_i(0)}e^{i\mathbf{Q}\mathbf{r}_j(t)}\right\rangle e^{-i\omega t}\end{aligned} \tag{2.4}$$

where $\langle ...\rangle$ denotes a quantum ensemble average. If we define the coherent cross-section as $\sigma_{coh} = 4\pi\langle b\rangle^2 = 4\pi b_{coh}^2$ and the incoherent cross-section as $\sigma_{inc} = 4\pi\langle b\rangle^2 = 4\pi b_{inc}^2$, then the scattered intensity in a neutron scattering experiment can be expressed in terms of coherent and incoherent contributions:

$$(\frac{d^2\sigma}{d\Omega d\omega}) = (\frac{d^2\sigma}{d\Omega d\omega})_{coh} + (\frac{d^2\sigma}{d\Omega d\omega})_{inc} \tag{2.5}$$

where σ is the cross-section and:

$$(\frac{d^2\sigma}{d\Omega d\omega})_{coh} = \frac{\mathbf{k}_{inc}}{\mathbf{k}_{scat}}\frac{\sigma_{coh}}{4\pi}S_{coh}(Q,\omega) \tag{2.6}$$

$$(\frac{d^2\sigma}{d\Omega d\omega})_{inc} = \frac{\mathbf{k}_{inc}}{\mathbf{k}_{scat}}\frac{\sigma_{inc}}{4\pi}S_{inc}(Q,\omega) \tag{2.7}$$

where $S_{coh}(Q,\omega)$ and $S_{inc}(Q,\omega)$ are the dynamic structure factors for coherent and incoherent scattering respectively [17].

Coherent scattering provides information on the collective effect arising from the interference of scattered waves by the atoms or molecules in the material over a large correlation volume. This gives an insight into the structure of the sample [20].

Incoherent scattering does not provide structural information, but contains information on the motion of single atoms (particularly hydrogen) which may be investigated by studying the changes in energy of the scattered beam. It relies on uncorrelated motions and provides insights into correlations among identical nuclei, thereby revealing information about the temporal evolution of individual atomic positions. It typically forms a flat background and can be effectively removed through empirical techniques with a high level of accu-

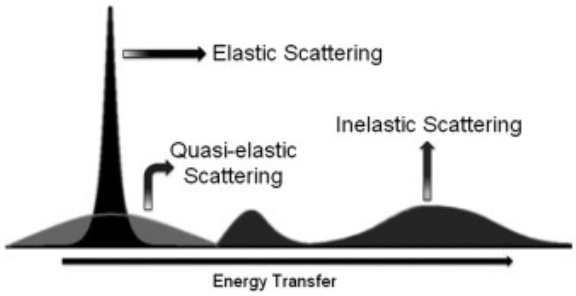

Figure 2.2: The elastic response of the system at $\hbar\omega$=0 provides information regarding the structure and appears as a broadened δ-like function due to the instrument resolution. This broadening captures only the dynamics within this timescale, while the quasi-elastic response at $\hbar\omega \approx 0$ corresponds to a further broadening of the elastic line and is associated with rotational and translational motions of the water molecules. The inelastic response ($\hbar\omega > 0$) probes the vibrations of the system [5, 10].

racy [20]. In a hydrated sample the incoherent scattering from the hydrogen atoms dominates, as its incoherent scattering cross section is of the order of $\sigma_{inc} = 80.26 \cdot 10^{-28} m^2$, much larger than any other element, meaning that most of the scattering signal for H arises from incoherent scattering, whereas coherent scattering forms part of the background.

Quasi-elastic scattering is a special case of incoherent scattering which arises from random rearrangements of the system due to thermal or quantum fluctuations between different configurations with the same energy [21]. The elastic line in a QENS experiment, shown in figure 2.2, might contain Bragg reflections. The broadening of this line comes from the instrumental resolution and is associated with rotational, vibrational and relaxational motions. In this case the energy transfers that characterize the system are small compared to the incident energy of the scattered neutrons [4]. It may also contain information on motions that are too slow to be captured by the instrumental resolution itself. In the quasi-elastic and inelastic part of the QENS spectrum, neutrons can either gain or lose energy after interacting with the sample. Measuring the energy transfer from the incident neutron to the sample, various phenomena such as diffusion, molecular rotations and other collective motions in the material can be investigated.

2.1.2 Quasi-Elastic Neutron Scattering

The information a QENS experiment can provide and the timescales that can be detected depend heavily on the energy and time resolution of the instrument. As already mentioned in the first part of §2.1, atomic motions take place in different time scales, leading to the need of carrying out several experiments with properly chosen resolution for some systems so as to qualitatively and quantitatively detect them all. If the instrument resolution is $\Delta(\hbar\omega)$, the resulting resolution-broadened spectrum will have a width larger than $\Delta(\hbar\omega)$ and the motions that can be detected, $\Delta(\hbar\omega)$, will have rates of the order of $\tau^{-1} \simeq \Delta(\hbar\omega)$. An ideal instrument would have a very narrow resolution, δ-like, in which all the motions would be seen as immobile. But the actual broadening of the resolution is the one that allows us to get insight into the different types of motions; slower motions will be hidden within the resolution function, while faster will contribute to the flat background. A high resolution instrument will provide more exclusive measurements and may not capture subtle features, while a low resolution instrument, although it can provide precise measurements, it can also introduce noise [20].

The measured dynamic structure factor S(Q,ω) from a QENS experiment can be described in general as:

$$S(\mathbf{Q},\omega) = EISF(\mathbf{Q})\delta(\omega) + [1 - EISF(\mathbf{Q})]\mathcal{L}(\mathbf{Q},\omega) \otimes R(Q,\omega) + B(\mathbf{Q}) \quad (2.8)$$

where EISF is the Elastic Incoherent Structure Factor, $\mathcal{L}(\mathbf{Q},\omega)$ is the Lorentzian function, $R(Q,\omega)$ is the resolution function of the instrument, which broadens the neutron scattering signal and $B(\mathbf{Q})$ is the background of the measurements.

The dynamics that characterize the confined water in clays can be determined by the analysis of the quasi-elastic part of the spectrum S_{QE} [6]. Considering the contributions from the translational, rotational and vibrational modes, the incoherent structure function can be written as [5]:

$$S_{inc}(\mathbf{Q},t) = S_{inc}^{trans}(\mathbf{Q},t) \otimes S_{inc}^{rot}(\mathbf{Q},t) \otimes S_{inc}^{vib}(\mathbf{Q},t) \quad (2.9)$$

In general, the analysis of the QE signal correlates to the relevant characteristic times associated with the water mobility [22, 23]. The combination of all these

parameters provide a total QENS spectrum of translational, rotational and vibrational motions and a sum of Lorentzians, which assume single exponential relaxation processes, are to be used for its analysis. The existence of an elastic component in the scattered intensity indicates the presence in the sample of a scatterer, the motion of which is essentially fixed in space [23], as its motion will not be able to be probed and will be seen as immobile. An important parameter that is obtained from the analysis of a QENS spectrum is the elastic incoherent structure factor (EISF), which provides information on the geometry and type of dynamics taking place in the sample. It is given by the formula:

$$EISF = A_0(Q) = \frac{I_{EL}(Q)}{I_{EL}(Q) + I_{QE}(Q)} \tag{2.10}$$

where $I_{EL}(Q)$ and $I_{QE}(Q)$ are the intensity of the elastic and quasi-elastic response respectively.

EISF is a key property to describe the dynamics of a system and in order to be calculated it requires the elastic and quasi-elastic part of the measured spectra to be distinguished from each other. A detailed investigation of the shape of the quasi-elastic part of the spectrum in regard to the elastic part, can yield precise information about the geometry of the scatterers. Particularly in the context of confined molecules, the type of confinement influences the local geometry of the molecule and the evolution of the EISF can give insight into the specific type of local restrictions on the molecule. Our samples were best described in terms of isotropic rotations, indicating that on a time average the molecules have no preferred orientation:

$$EISF = A_0(Q) = p_{rc} + (1 - p_{rc}) \times \left[\left(\frac{sin(Qa_{rc})}{Qa_{rc}} \right)^2 \right] \tag{2.11}$$

where p_{rc} is the fraction of immobile photons and a_{rc} is the radius of rotation.

2.2 Free Diffusion, Jump Diffusion and Minimalistic Models

As already noted, the analysis of a QENS spectrum gives insight into the diffusive motions, as well as the correlation times, of the molecules in the sample. There are different models able to describe such dynamics depending on the kind of the motion and can be described using free and jump diffusion models.

A **free diffusion model** can be described by a Brownian motion. In this case after a collision with a neutron at t=0, the particle changes direction and speed so that the initial collision conditions are lost. For small Q-values this transition can be seen as continuous and described by Fick's law [24]:

$$\frac{\partial G(\mathbf{r},t)}{\partial t} = D_t \nabla^2 G(\mathbf{r},t) \tag{2.12}$$

where D_t is the translational diffusion coefficient and $G(\mathbf{r},t)$ is the self-correlation function. Solving Fick's law results in a Lorentzian line in energy [17]:

$$S(\mathbf{Q},\omega)^{trans} = \mathcal{L}(\mathbf{Q},\omega) = \frac{1}{\pi}\frac{\Gamma(\mathbf{Q})}{\Gamma(\mathbf{Q})^2+\omega^2} \tag{2.13}$$

where $\Gamma(\mathbf{Q})$ is the HWHM and equals to: $\Gamma(\mathbf{Q}) = D_t|\mathbf{Q}|^2 = D_t Q^2$ resulting in the famous "DQ^2" law or the free diffusion model (FDM).

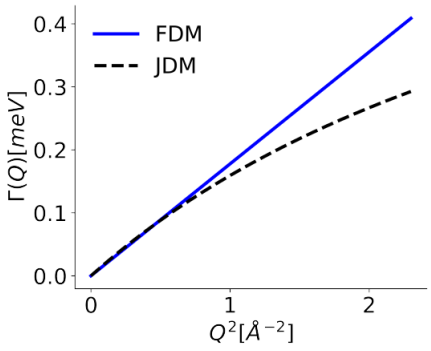

Figure 2.3: Evolution of the half width at half maximum (HWHM), aka. $\Gamma(Q)$, with Q^2 for the free and jump diffusion models. The free diffusion model (FDM) shows the expected linear dependence as indicated in eq.(2.13), while the Singwi-Sjölander model (SSM) follows the eq.(2.14) rule.

In the contrary, for large Q-values, there is the assumption that a particle remains on the initial site for a residence time τ_0, showing rotational motions and then jumps to the new location. This translation is called jump diffusion and is different from the DQ^2 law. There are several jump diffusion models, such as the Singwi-Sjölander model, the Chuddley-Elliot model and the Hall Ross model, but only the ones used in this analysis are going to be presented.

The first one is the **Singwi-Sjölander model** (SSM) [1]. In this case the Q-dependence of the HWHM changes as:

$$\Gamma(\mathbf{Q}) = \frac{D_t|\mathbf{Q}|^2}{1 + D_t|\mathbf{Q}|^2\tau_0} \tag{2.14}$$

where $D_t = \frac{\ell^2}{6\tau_0}$ is given in terms of the mean-square jump length ℓ^2 and residence time τ_0. Appendix 6.1 shows the derivation of the equation used for the analysis of the data considering the convertion factors.

Another model used for the analysis of the diffusion processes is the **Chudley-Elliot model** (CEM). In this case the reorientational motions are described by:

$$\Gamma(Q) = \frac{\hbar}{\tau_0}\left(1 - \frac{sin(Q\ell)}{Q\ell}\right) \tag{2.15}$$

The difference between these two diffusion models lies on the fact that the CEM and its' sinusoidal behavior implies that as the water molecules makes a discrete jump, it ends up within a different environment than before, like two communicating potential wells, while for the SSM the molecule remains within the same potential [25].

Regarding the **minimalistic model** (MM), it is another way to analyze S(**Q**,ω) without relying on Lorentzians to capture specific dynamics of a system [9, 26, 27, 28]. Through the application of the Van-Hove formalism, the dynamic structure factor, denoted as S(**Q**,ω), can be expressed in terms of momentum and time as F(**Q**,t) via a Fourier transformation. Similarly, employing a second Fourier transformation enables the representation of S(**Q**,ω) in terms of space and time as G(**r**, t) [17]:

$$S(\mathbf{Q},\omega) = \frac{1}{2\pi}\int_{-\infty}^{\infty} dt e^{-i\omega t}F(\mathbf{Q},t) = \frac{1}{2\pi}\int_{-\infty}^{\infty} dt \int d^3r e^{i(\mathbf{Qr}-\omega t)}G(\mathbf{r},t) \tag{2.16}$$

The momentum-time correlation function, which is the Fourier transform of the Van Hove formalism can be written in a generic form as:

$$F(\mathbf{Q},t) = (1 - EISF(\mathbf{Q}))\phi(\mathbf{Q},t) + EISF(\mathbf{Q}) \tag{2.17}$$

where the quasielastic and elastic contribution are being separated respectively. ϕ(**Q**,t) is the atom-averaged normalized self-correlation function, describing the relaxation of the hydrogen atoms [26, 28]. This generic form of the $F(\mathbf{Q},t)$ is assumed to have a (symmetrized) relaxation function of the form of a stretched Mittag-Leffler function:

$$\phi_{ML}^{(+)}(t) = E(-(|t|/\tau)^{\alpha}) \tag{2.18}$$

which can be considered a generalization of the exponential function. We note that,

$$E_{\alpha}(z) = \sum \frac{z^n}{\Gamma(\alpha n + 1)} \tag{2.19}$$

is an entire function in the complex plane, where Γ is the generalized factorial and that the exponential function is retrieved in the special case of $\alpha = 1$. Here α sets the form of the relaxation function and τ its time scale. For 0<α<1 the stretched ML function takes a scale-invariant power law form,

$$\phi_{ML}^{(+)}(t)\ \frac{(t-\tau)^{-\alpha}}{\Gamma(1-\alpha)} \tag{2.20}$$

and since $\lim_{z\to 0}\Gamma(z) = \infty$, this long time tail will vanish for $\alpha \to 1$, i.e. for exponential relaxation. The Q-dependent parameters in the above model are thus α, determining the form of the relaxation function, τ, setting the time scale and the EISF [29].

This method will be used to benchmark the behavior of bulk water as a function of temperature.

Materials and Methods

3

3.1 Samples

3.1.1 Bulk Water Samples

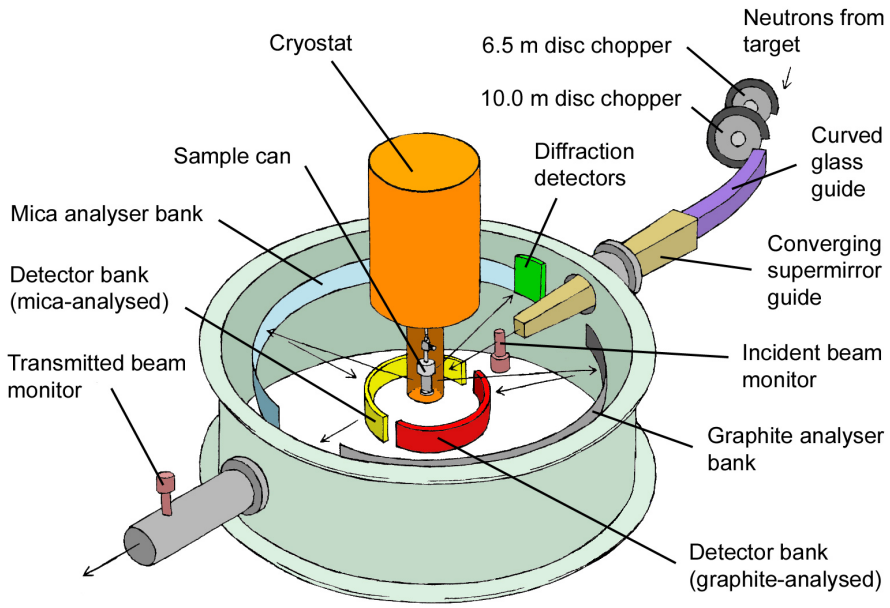

Figure 3.1: Schematic of the backscattering IRIS spectrometer at the ISIS facility in UK. IRIS is a time-of-flight inverted-geometry crystal analyzer spectrometer designed for quasi-elastic and low-energy high resolution inelastic spectroscopy [30].

The bulk-water data were collected using the backscattering IRIS spectrometer installed at the Spallation Neutron and Muon source at the ISIS facility in UK. **IRIS** is a cold neutron indirect backscattering spectrometer. In such kinds of spectrometers, while the initial energy E_i of the incident neutrons varies, the final energy E_f is fixed. The incident wavelength of the neutrons is λ= 6.3 Å and the energy resolution of the spectrometer is ΔE= 17.5 μeV. The samples were mounted in cylindrical sample holders and measurements were

conducted for the temperatures 280, 290, 300 and 310 K by Dr. Mark T. F. Telling.

3.1.2 Clay Mineral Samples

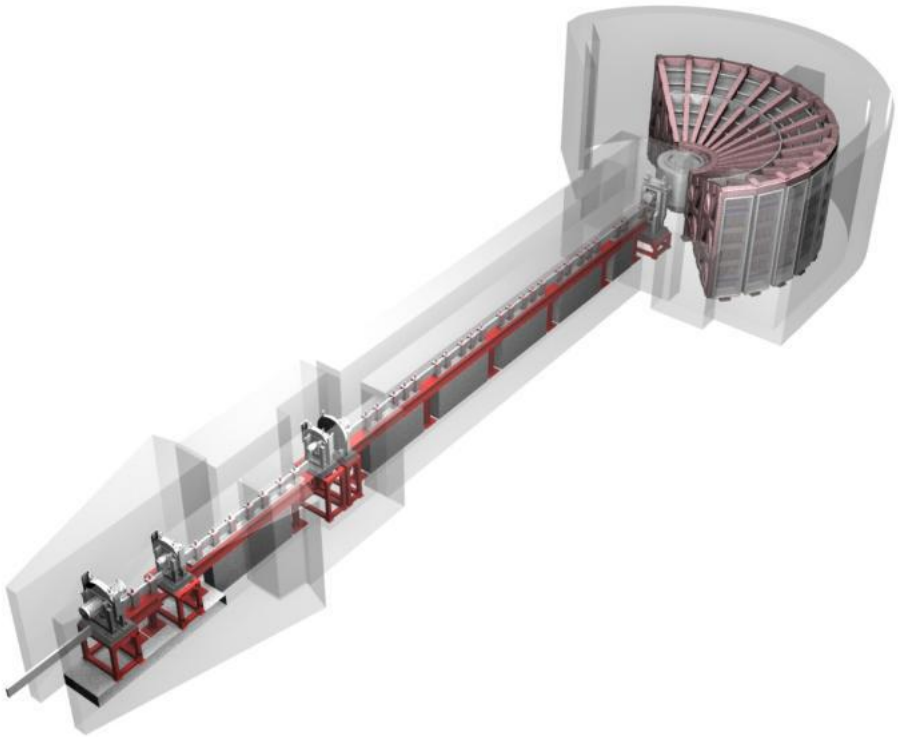

Figure 3.2: Schematic of the disk-chopper-type AMATERAS spectrometer at the Spallation Neutron Source of J-PARC in Japan [31, 32].

The clay mineral data of Mt was collected using the time-of-flight AMATERAS spectrometer installed at the Spallation Neutron Source at the Material and Life Science Experimental Facility (MLF) of J-PARC in Japan. **AMATERAS** is a cold neutron direct geometry time-of-flight spectrometer (ToF). In this case the initial incident neutron energy E_i remains fixed using a chopper system and the final energy E_f is measured through the time of arrival of the neutrons after interacting with the sample [31, 32]. The data in this case were collected using an incident neutron beam with λ=5.2 Å, corresponding to an incident energy of E_i= 3 meV, while the instrument's resolution was ΔE=54 μeV [9]. The neutron scattering experiment at J-PARC was performed under the J-PARC Long-Term Proposal (proposal no. 2018L1000) by other members of the neutron and X-ray scattering group.

The oriented clay films prepared for this experiment by Associate Profes-

sor Will P. Gates from Deakin University in Australia, were firstly dehydrated in an oven and then re-hydrated adding either deionized water or saline water. The first NaMt sample had an oven dried mass of 0.5503g and then 0.165 mL deionized water was added and the second NaMt sample had an oven dried mass of 0.5338g and then 0.160 mL of 0.5M NaCl was added. The third sample was CaMt with an oven dried mass of 0.8084g and 0.243mL of 0.5M $CaCl_2$ was added afterwards. The samples were prepared in order to observe if and how the inclusion of salt in the sample affected the diffusion of the water molecules under electric field stimulation.

Here, the percent Gravimetric Water Content(GWC) of the re-hydrated clay samples was also calculated through the equation:

$$GWC = (\frac{m_{wet} - m_{dry}}{m_{dry}}) \cdot 100 \tag{3.1}$$

where m_{wet} is the mass of the clay after re-hydration and m_{dry} is the oven dried mass and the overall results are shown in Table 3.1.

Table 3.1: Measured gravimetric water content for the NaMt and CaMt samples.

Samples	m_{dry} [g]	m_{wet} [g]	GWC [wt%]
NaMt DIW	0.5503	0.7153	29.98
NaMt 0.5M NaCl	0.5338	0.6891	29.09
CaMt 0.5M $CaCl_2$	0.8084	1.038	28.40

3.1.3 EF-Sample Holder

Similar to the approach employed by Ignazzi et al. [6], considering that electrical stimulation of clay minerals is not a common practice in neutron spectroscopy, a dedicated electric field sample holder was used in this case as well during the QENS experiments.

The design of the sample holder was performed by Professor Heloisa N. Bordallo and Dr. Yukinobu Kawakita and fabricated by the Niels Bohr Institute Technical Support Group in the Mechanical Department of the University of Copenhagen and is depicted in Figure 3.3a. Alluminum alloy 5083, containing Al, Mg and Mn in different concentrations, was the main component for the

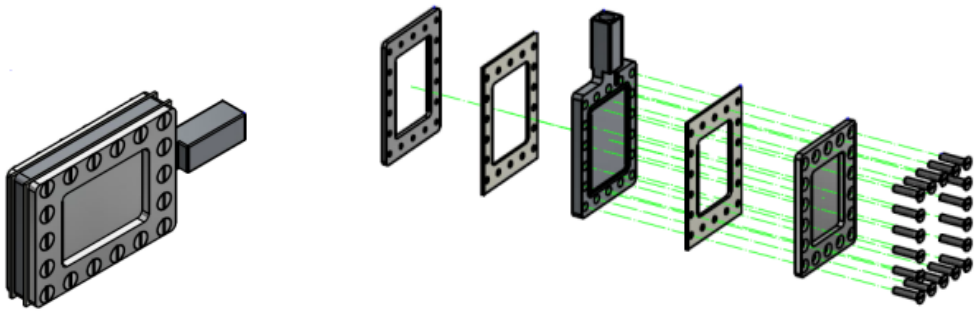

(a) Schematic of the EF-sample holder.

(b) Details into the different parts the sample holder is composed of.

Figure 3.3: Schematic of the dedicated EF-Sample Holder used for the QENS experiments in AMATERAS designed by Dennis Westphal Wistisen from Niels Bohr Institute.

aluminum parts of the sample holder. Teflon was used to seal the base and electrically insulate the lid of the cell from its body (Figure 3.3b). The space between the sample holder and the lid was 4mm and the total length of the sample holder with the lid was 90mm.

3.2 Data Analysis

3.2.1 Mantid Software: Bulk-water data analysis

Mantid is a software for the reduction and analysis of neutron scattering and muon spectroscopy data [8]. Regarding bulk-water, the vanadium run was used to calibrate the data collected using the backscattering spectrometer and measure the resolution of the instrument because of its' ability to scatter neutrons elastically, as all detectors should ideally do. For the correction of the signal there should also be an empty can subtraction. A note to underline here is that for the bulk water data, the empty can's intensity measurement was too high and subsequently was not subtracted. After calibrating the data they were transformed into the dynamic structure factor S(Q,ω) and for further treatment they were grouped in 9 subgroups of the scattering vector, Q, ranging from 0.55 to 1.85 Å^{-1}.

3.2.2 Python Software: Benchmarking bulk-water data as a function of temperature

Another way to treat the QENS data was to use a python script, specifically written for the minimalistic model analysis [9]. In contrast to more traditional modelling of the data through the analytical models which require prior information of the system, since it is essential to attribute each Lorentzians needed to represent the dynamics to a specific motion, this model can capture the full dynamics of the confined water without any prior information [29]. The analysis was done in four steps, as described thoroughly in [33]:

1. First the energy transfer, ω, axis is symmetrized, so that there are as many positive as negative values. Then, the dynamic structure factor is symmetrized using the detailed balance condition $S(Q,\omega) = exp(\beta\hbar\omega)S(Q,-\omega)$, so that positive ω values represent the energy loss and negative ω values the energy gain of the neutrons. Following that, the angular and frequency normalization of the spectra is done; the first one corrects the Q-dependent variation by using the vanadium, while the second assures the condition $\int_{-\infty}^{+\infty} S^{(+)}(Q,\omega)\,d\omega = \int_{\omega_{min}}^{\omega_{max}} S^{(+)}(Q,\omega)\,d\omega = F^{(+)}(Q,0) = 1$ is fulfilled. The uncertainties for $S^{(+)}(Q,\omega)$ are estimated using error propagation.

2. Then the intermediate scattering function is computed and deconvoluted. A discrete inverse Fourier transform is used and the symmetrized and normalized intermediate scattering function is found. The uncertainties are estimated through Fourier transform by considering the uncertainties of $S^{(+)}(Q,\omega)$ are Gaussian distributed.

3. Fitting the simple model. In this step, the intermediate scattering function $F(Q,t)$ is fitted to find the EISF and the other fit parameters through the model described by eq.2.17.

4. Create a fitted model F(Q,t) from the fit parameters.

3.2.3 Dave Software: Oriented clay-films

For the water confined in the clay minerals, a similar procedure with that of bulk-water was followed, but in this case using a built-in reduction software in AMATERAS, called UTSUSEMI [34]. After the calibration of the data with the vanadium run and the subtraction of the background, the scattering vectors were grouped in 7 subgroups with 0.4$\leq Q \leq$1.6 Å^{-1}. Then they were transformed into the dynamic structure factor S(Q,ω) and further treated with the **Dave Software** [15]. This software is used for an equivalent data manipulation as Mantid and UTSUSEMI, but in our case was only used for the analysis of the QENS spectra and the graphical masking of the detectors that contained Bragg reflections.

3.2.4 Details in the Analysis of the Data

Following the normalization and calibration of the data is the width analysis of the QENS spectrum. After fitting each spectrum with the suitable function, a linear background and a δ-function [10], we can obtain the HWHM of the function we have used. In our case the most suitable function to describe the broadening of the spectrum was a Lorentzian function. Of course, other functions, such as Gaussians, can be used for the interpretation of the data, but Lorentzians are more often used because they more accurately represent the broadening and asymmetry of the experimental data. The Lorentzian was used to capture and describe the dynamics, the linear background to exclude any residuals from the fitting and the resolution function to interpret the elastic part of the spectrum. In the case of the clay mineral oriented films, though, equation 2.8 appeared to give rise to a poor fitting quality and therefore an additional QE component was introduced including a second Lorentzian as follows [22]:

$$S_m(Q,\omega) = F\left[[A_0(Q)\delta(\omega) + A_1(Q)L_1(\Gamma_1,\omega) + A_2(Q)L_2(\Gamma_2,\omega)] \otimes F(Q,\omega)\right] + B(Q) \tag{3.2}$$

where F is a scalling factor, A_i are the structure factors with A_0(Q) representing the effective EISF, $L_i(\Gamma_i,\omega)$ are the Lorentzian functions having HWHM at Γ_i and F(Q,ω) is the experimental resolution function.

Then, the dependence of the width on the momentum transfer (Q) is in-

vestigated, and an appropriate diffusion model is employed to fit the resulting curve, thereby obtaining the diffusion coefficient. According to the user guide of the Peak Analysis (PAN) program in Dave software [35] the plot of the residuals provides a visual goodness of the fit besides the χ^2-value. The residuals are defined as:

$$r_i = \frac{MEAS - FIT}{\sigma_i} \tag{3.3}$$

where σ_i are the uncertainties on the data points, MEAS are the measured data points and FIT are the fitted data points. If the data have been modeled well, then the residuals should vary between ± 1, as shown by the horizontal dashed lines.

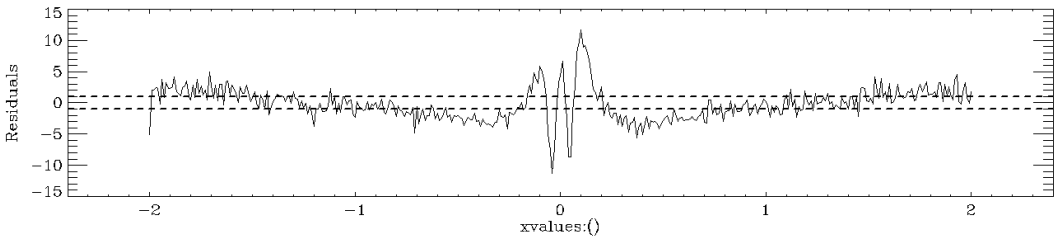

(a) Residuals with 1 fitted Lorentzian at Q=1 Å^{-1}.

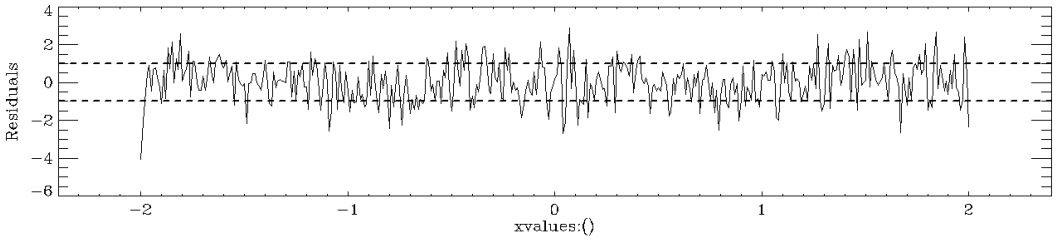

(b) Residuals with 2 fitted Lorentzians at Q=1 Å^{-1}.

Figure 3.4: Residuals of the fitting with one and two Lorentzians respectively. As seen from the figures, in order to eliminate the noise and to accommodate an asymmetrical fitting, applying two Lorentzians instead of one was unavoidable.

4 Results

4.1 Analysis of Bulk-Water samples

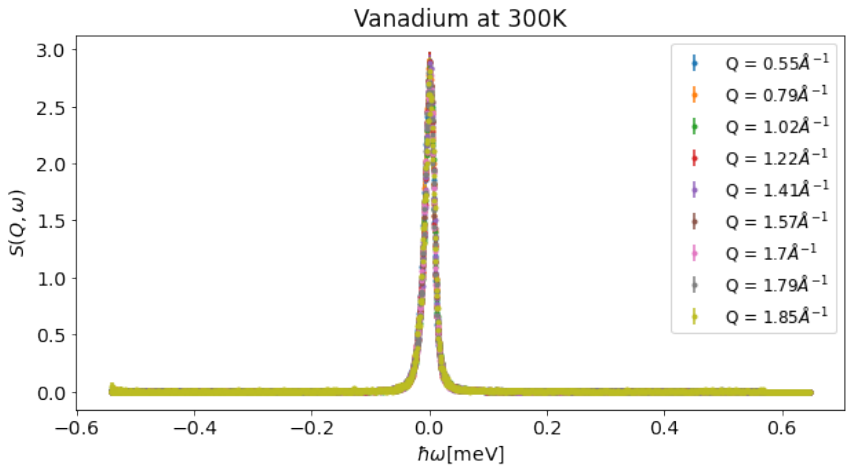

(a) Vanadium Run of Bulk Water at 300K.

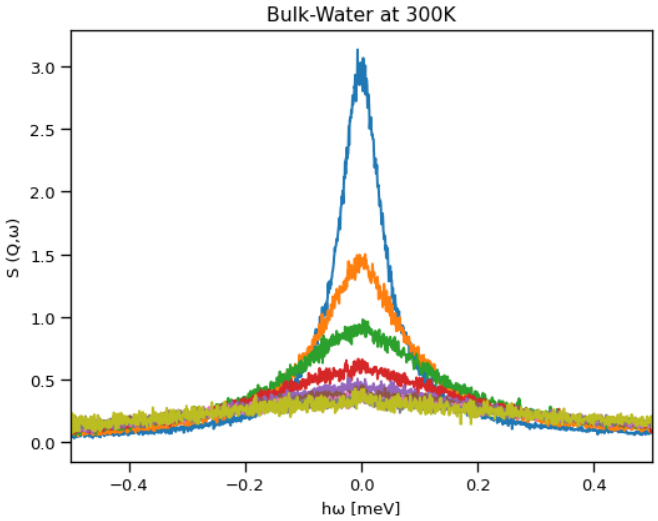

(b) QENS spectra of Bulk Water at 300K.

Figure 4.1: Overview of the QENS data for bulk-water as a function of momentum transfer ω, collected using the IRIS spectrometer at ISIS at 300 K. (a) Vanadium spectra defining the resolution function and (b) Reduced bulk-water spectra showing an evident Q-dependence.

In Figure 4.1a and 4.1b the vanadium run and the reduced QENS data of bulk-water at 300K are shown respectively. For better treatment of the data, they were grouped in 9 Q-subgroups of the scattering vector ranging from 0.55 to 1.85 $Å^{-1}$. As seen from Figure 4.1b, as the Q-values increase, the elastic response decreases and the broadening of the QE-response becomes more apparent. This happens because while the Q-values increase, the d-spacing becomes consequently smaller (according to Bragg's law: $Q=\frac{4\pi sin(\theta)}{\lambda}=\frac{2\pi}{d}$), so that the scatterers, in this case the hydrogen atoms, are essentially located in the probed Q-space and the velocity of its protons cannot be resolved anymore and ends up as background. In the contrary, for infinite probing time, i.e. small Q-values, the molecules are moving much slower relative to the time window probed by the spectrometer.

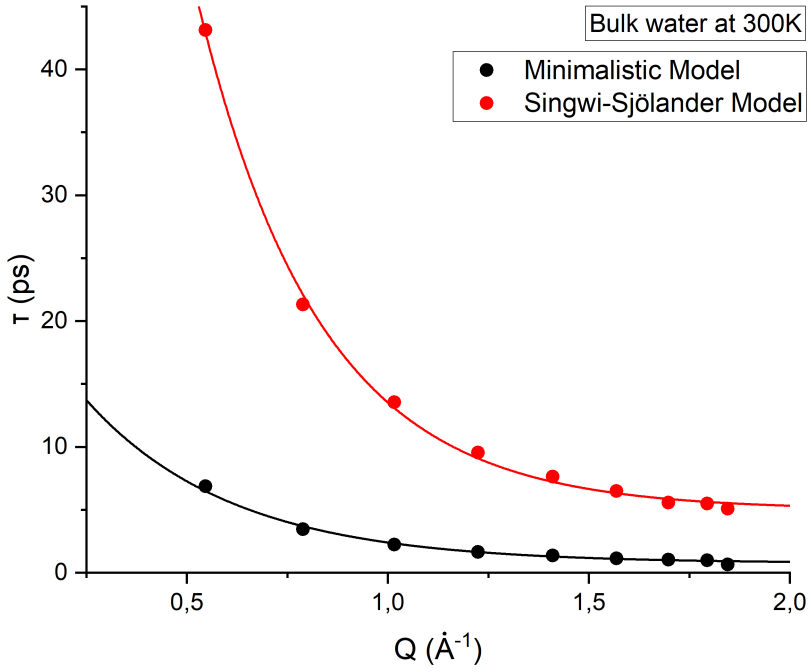

Figure 4.2: The evolution of τ with Q for the SSM and MM at 300K. From the τ values and their errors, which are small enough to not be visible in the figure, we can calculate the HWHM for the minimalistic model through the equation: $HWHM=\frac{\hbar}{2\tau(Q)}$.

Figure 4.2 shows the Q-dependence of τ. Both models show, as anticipated, a decaying exponential dependence of the τ with Q. As the momentum transfer increases, the probed timescales become shorter; the highest Q-values corre-

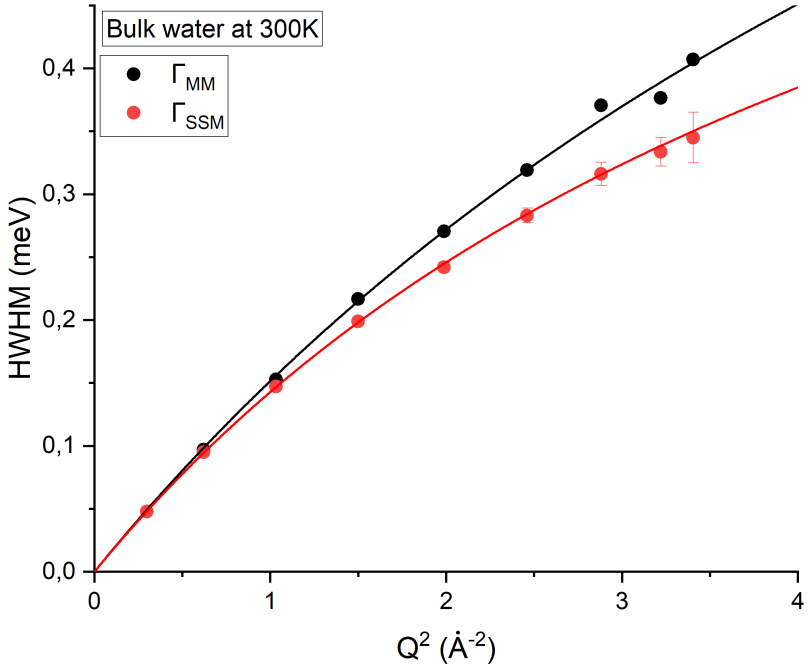

Figure 4.3: The HWHM dependence on Q^2 at 300K. From the evolution of $\Gamma(Q^2)$ it is observed that the SSM best fits the data. From the fitting of the curves with eq. 2.14, the diffusion coefficient and residence time with their errors are obtained. The values are in good agreement with each other as well as with bibliography and shown in table 4.1.

spond to local reorientational motions which are faster relaxation processes than the one probed at low Q-values that have to do more with diffusive motions. For the SSM we obtained a value of τ_{SSM}=0.49 $\pm$ 0.05 ps, from Mantid the value was τ_{Mantid}=0.44 ps directly from the fitting, while for the MM the equivalent value was τ_{MM}=0.74 $\pm$ 0.01 ps. Using the equation HWHM=$\frac{\hbar}{2\tau(Q)}$, the HWHM with the respective errors can be calculated. The results are shown in figure 4.3. This figure shows the evolution of the HWHM with Q^2, whose curvature confirms that the SSM is the model that best fits the acquired data for the bulk-water. In this step, from the slope of the line tangent to the curve the diffusion coefficient was obtained as indicated in eq. 2.14 with a value of D_t=2.6 $\pm$ 0.09 10^{-9} m^2/s for the SSM and D_t=2.59 $\pm$ 0.01 10^{-9} m^2/s for the MM.

In Table 4.1 all values of D_t and τ with their errors for all four temperatures and all three fitting models are provided. As seen, each parameter in each temperature is comparable between the methods, a result that confidently allows

us to confirm that all three methods provide reasonable fits. The reason why the Mantid fitted values do not have error bars is due to the Mantid software which calculated the values of the different parameters without any errors from the fitting of the provided model. Several studies done so far mainly at room temperature have shown results that are in agreement with the ones provided in this study. Mills in 1973 [11], Chen et al. in 1982 [10] and Price et al. in 1999 [12] are only some of the former studies done on bulk water, whose results for 300K are in agreement and calculated as D_t=2.3 10^{-9} m^2/s. More recent studies have also calculated $D_t \approx 2.3\ 10^{-9}$ m^2/s [13, 14]. Future users are now provided with three different approaches to confirm the results of their analysis and choose the best that fits them for further investigation.

Table 4.1: Diffusion Coefficients and Residence Times: Obtained values of the self-diffussion coefficient D_t and residence time τ of bulk-water as a function of temperature using three different approaches to analyze QENS data. All values are comparable to each other for the respective temperatures as well as with the bibliography [10, 11, 12, 13, 14].

Temperature	280K	290K	300K	310K
D_t^{SSM} (10^{-9} m^2/s)	1.66±0.03	2.06±0.03	2.6±0.09	3.16±0.2
D_t^{Mantid} (10^{-9} m^2/s)	1.65	2.1	2.54	3.02
D_t^{MM} (10^{-9} m^2/s)	1.53±0.05	2.07±0.03	2.59±0.01	3.07±0.02
τ^{SSM} (ps)	0.98±0.08	0.63±0.03	0.49±0.05	0.38±0.07
τ^{Mantid} (ps)	0.99	0.67	0.44	0.31
τ^{MM} (ps)	0.89±0.07	0.91±0.07	0.74±0.01	0.59±0.03

Final step on the interpretation of the bulk water data is to plot the diffusion coefficient D_t derived from each model as function of the four temperatures. To examine the impact of temperature, an Arrhenius plot was employed:

$$ln(k) = -\frac{E_a}{R}\frac{1}{T} + ln(a) \tag{4.1}$$

where k is a rate constant, E_a the activation energy, T the temperature and a is an empirical constant. The activation energies were found to be $E_a \approx 16 \pm 0.18$ kJ/mol for the MM and $E_a \approx 15 \pm 0.06$ kJ/mol for the SSM, which are in good agreement with each other as well as with the so far existing literature [11, 36] ($E_a \approx 18$ kJ/mol).

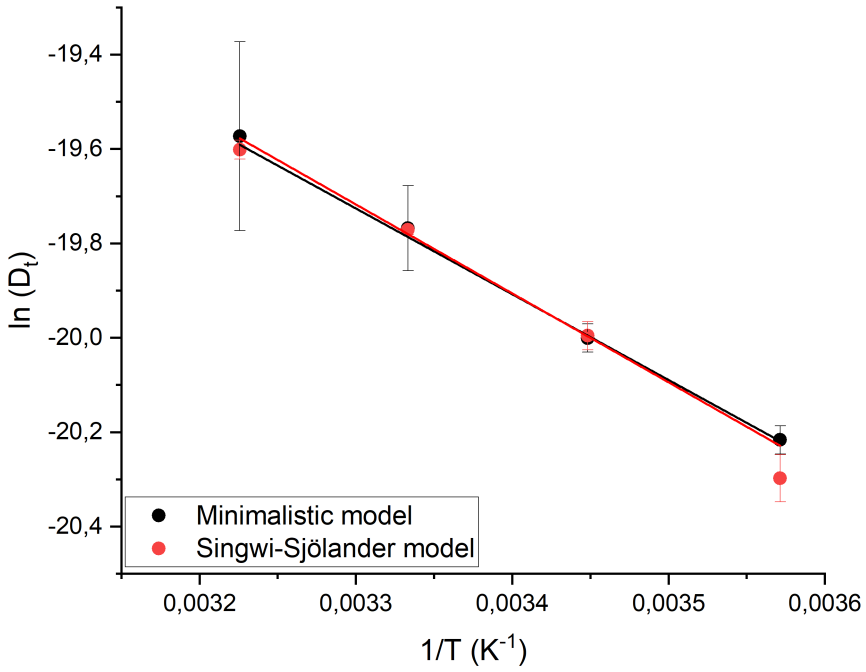

Figure 4.4: Rate of the derived diffusion coefficient with temperature for the SSM and MM. Fitting the linear dependence with eq.4.1 we obtained the activation energy for self-diffusion free water to be $\approx 16 \pm 0.18$ kJ/mol for the minimalistic model and $\approx 15 \pm 0.06$ kJ/mol for the Singwi-Sjölander model.

4.2 Clay Minerals

4.2.1 Sodium Montmorillonite NaMt

The first set of samples to be studied was oriented films of hydrated NaMt (figure 4.5), in order to observe whether or not changes in the applied voltage or in the salinity concentration had any effects on water mobility. The first NaMt sample includes 0.165mL deionized water (29.98% GWC) and has been subjected to 0 and 40V electrical field stimulations, while the second NaMt oriented film includes 0.160mL of 0.5M NaCl (29.09 % GWC) and has been studied at 0 and 50V applied electrical field.

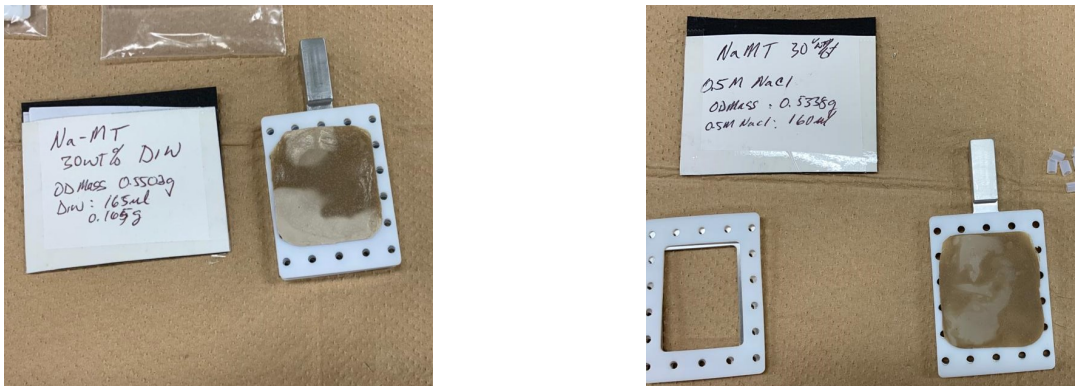

(a) NaMt with 0.165 mL deionized water.

(b) NaMt with 0.160 mL of 0.5M NaCl.

Figure 4.5: Prepared NaMt samples in their sample holders.

The 7 Q-subgroups for the 0V data of NaMt hydrated with deionized water (DIW) are depicted in figure 4.6. For both 0 and 40 V, three bragg (hkl) reflections were noticed at Q=0.4, 1.2 and 1.4 $Å^{-1}$, which arose from the neutron scattering from the structure of the clay. In the inset figure the total fitting at Q=1 $Å^{-1}$ is shown. The fitting required using a δ-function as the resolution function (green dashed line), a linear background (purple solid line) and two Lorentzian functions (a narrow one indicated with a magenta dashed line and a broad one indicated with an orange dashed line). The need to use two Lorentzians resulted from the poor fitting and the large residuals that were obtained after using only one Lorentzian fit (see Materials and Methods: §3.2.4). This indicates that the instrument resolution enabled us to detect more than one water population, and maybe more complex motion of the

water molecules confined in the pores of the clay mineral. The same fitting procedure was done for both samples, at all other Q-values and for all applied EFs.

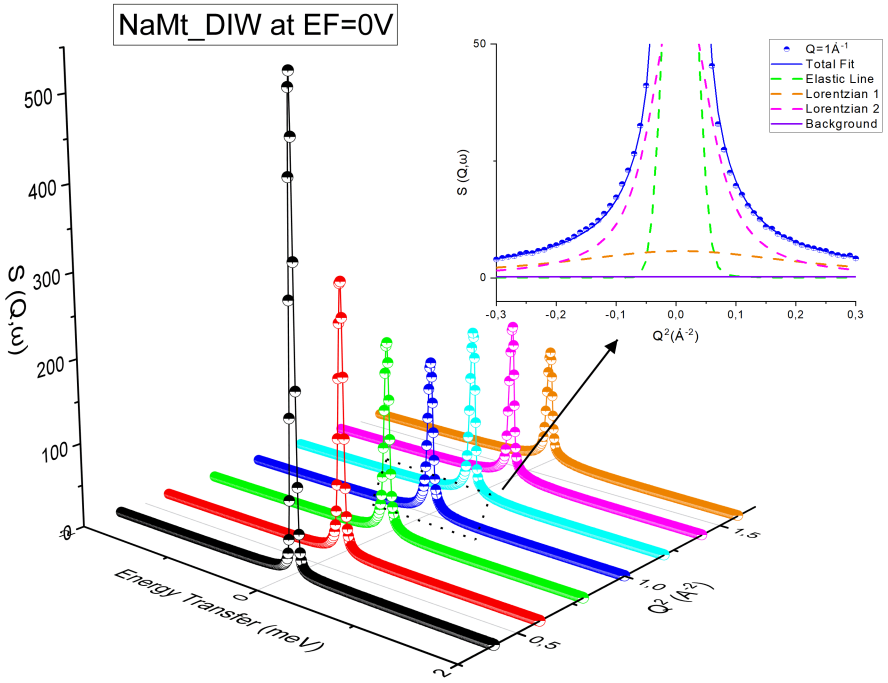

Figure 4.6: QENS spectra at EF=0 V for the unsalted NaMt sample at 0.4 to 1.6 Å^{-1} Q-values. Inset: Total fitting of the spectrum at Q=1 Å^{-1} with a resolution function (green dashed line), 2 Lorentzian functions (narrow one: magenta dashed line and broad one: orange dashed line) and a linear background (purple solid line).

Exporting the HWHM from the fitted QENS spectra of the narrow lorentzian for the DIW and 0.5M NaCl NaMt samples and plotting them against Q^2 showed the dependence shown at the top panels of figures 4.7 and 4.8 respectively, which were ideally fitted with the SS model and the parameters obtained were the diffusion coefficient D_t and the residence time τ. The fitting of the broader lorentzian was done using the CE model described in §2.2 and is shown at the bottom panels of the same figures. From the fitting we obtain the residence time τ and jump length ℓ. During the fitting process the Q-values at 1.2 and 1.4 Å^{-1} were excluded. The final results for both samples and EF applications are shown in tables 4.2 and 4.3, while the errors of the parameters not derived from the fittings were calculated through error propagation. From the results of both tables we can conclude that the D_t of the samples does not appear to

be affected neither by EF application nor by salt inclusion with respect to the error values.

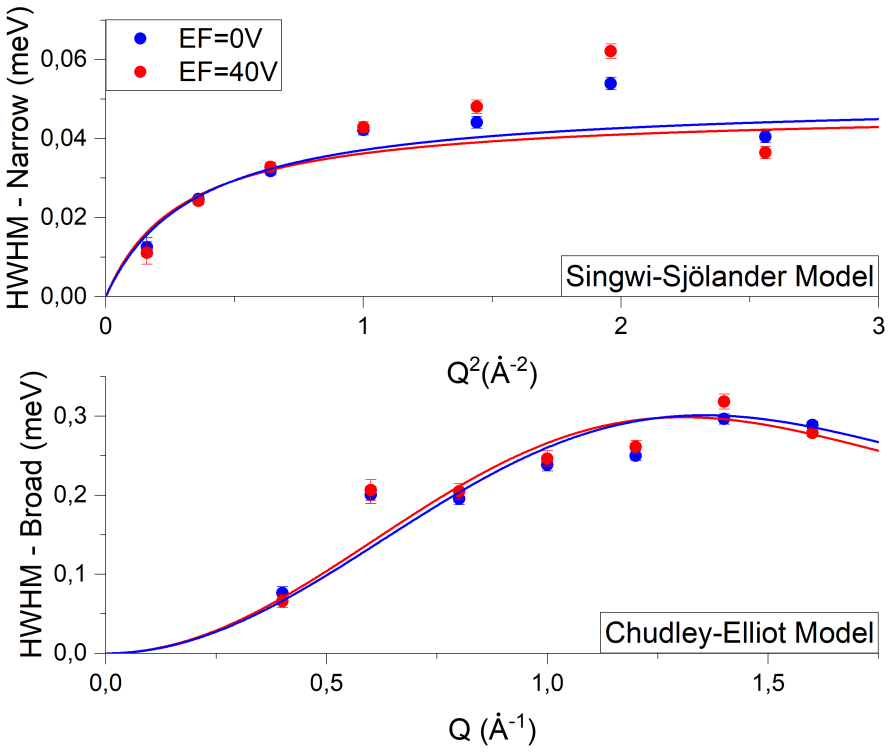

Figure 4.7: Fitting results of the two Lorentzians found in the deionized NaMt clay mineral spectra. The fitting of the narrow Lorentzian (upper panel) was done using the Singwi-Sjölander jump diffusion model and the derived parameters are the diffusion coefficient D_t and the residence time τ. The fitting of the broader Lorentzian (lower panel) was done using the Chudley-Elliot diffusion model and the derived parameters are the residence time τ and the mean length jump ℓ.

Regarding the derived residence times τ, the values do not change with respect to the error values as well. This indicates, that no matter the kind of the motion (slow or fast), the time spent on each discrete location of the molecule does not really change. Observing the parameters in table 4.2, although τ remains at the same rate within error, we can see that ℓ changes. For example, when NaCl is included in the sample, the slower diffusion is compensated for its' slower speed by jumping a shorter distance while residing at each new location for the same amount of time as the faster one. This way both diffusion rates are able to reside for the same amount of time and according to their diffusion rate, they have a larger or smaller jump length.

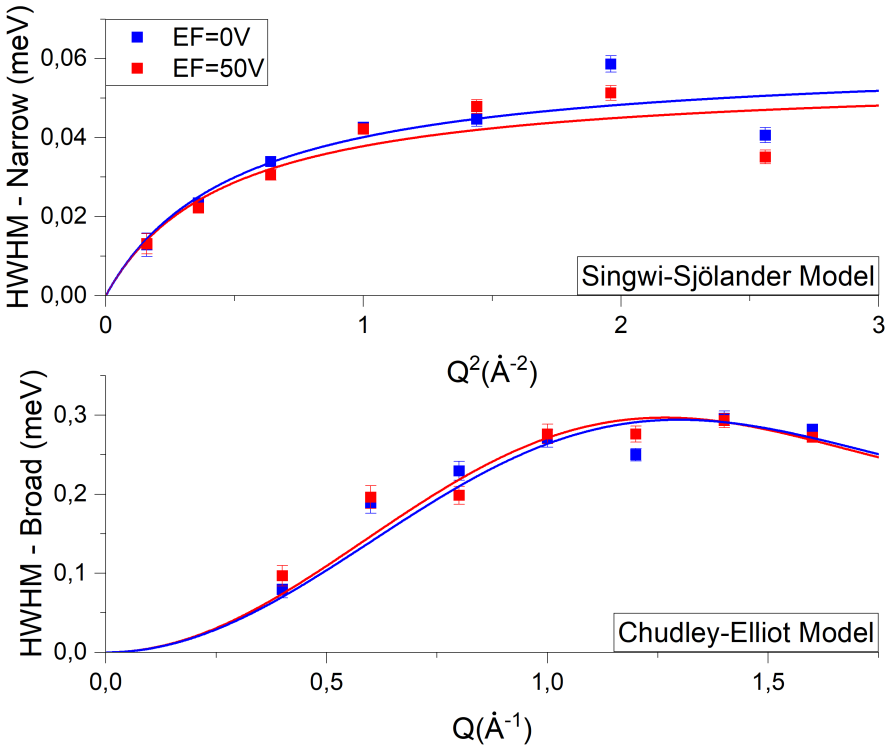

Figure 4.8: Fitting results of the two Lorentzians found in the salted NaMt clay mineral spectra. The fitting of the narrow Lorentzian (upper panel) was done using the Singwi-Sjölander jump diffusion model and the derived parameters are the diffusion coefficient D_t and the residence time τ. The fitting of the broader Lorentzian (lower panel) was done using the Chudley-Elliot diffusion model and the derived parameters are the residence time τ and the mean length jump ℓ.

Table 4.2: Results for the diffusion coefficient for the narrow Lorentzian at both 0 and 40 V, as well as salted and unsalted samples. The results clearly indicate that neither the application of electric field stimuli nor the presence of salt exert any influence on the dynamics of the fitted narrow population.

Parameters	DIW(0V)	DIW(40 V)	NaCl(0 V)	NaCl(40 V)
D_t (10^{-9} m^2/s)	2.2±0.5	2.4±0.9	1.7±0.5	1.8±0.6
τ (ps)	13.1±1.5	13.9±2.3	10.8±1.5	11.8±1.9
ℓ (Å)	13.15±0.2	14.15±0.2	10.49±0.2	11.29±0.1

Table 4.3: Results for the diffusion coefficient for the broad Lorentzian at both 0 and 40 V, as well as salted and unsalted samples. It is obvious from the results that neither electric field stimuli nor the presence of salt affect the dynamics of the fitted broad population at the resolution windows used herein.

Parameters	DIW(0V)	DIW(40 V)	NaCl(0 V)	NaCl(40 V)
τ (ps)	4±0.2	4.1±0.2	4.1±0.2	4.1±0.1
ℓ (Å)	3.3±0.2	3.4±0.2	3.7±0.2	3.6±0.1

In order to interpret the data accurately, confirm our observations from the fitted QENS spectra and get an insight on the time scales of the different motion populations, we calculated and plotted the susceptibility. Plotting of the susceptibility allows interpreting the data without the need of a fitting process beforehand. As seen from figure 4.9, which includes the untreated data, we clearly have evidence of multiple dynamical processes confirming that the second Lorentzian that was observed during the fitting procedure was real signal. Two motions, the slowest one associated with the Q-dependent maximum and the faster one associated with a visible tail, have a crossover point at ≈ 55 ps when no EF is applied and at ≈ 69 ps when EF of 40V is applied, both of which are within the ps-scale.

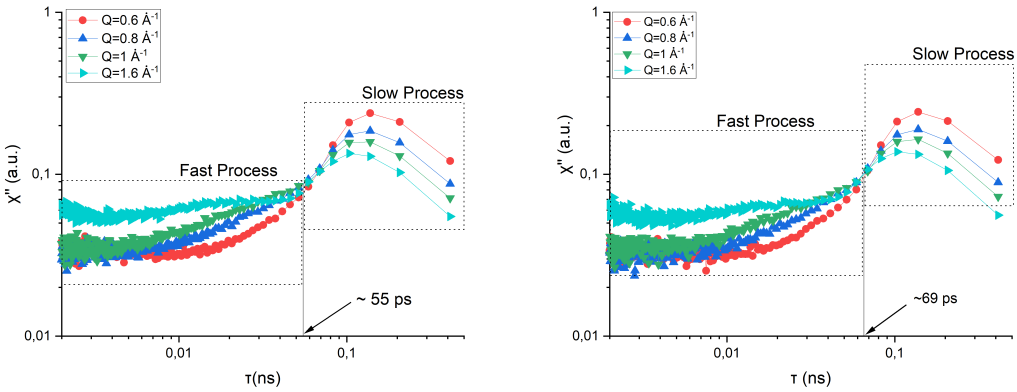

(a) Susceptibility at EF=0V for the deionized NaMt oriented clay mineral film. The slower and faster dynamics are dissociated at ≈ 55ps.

(b) Susceptibility at EF=40V for the deionized NaMt oriented clay mineral film. In this case the two dynamic processes are seperated at ≈69ps.

Figure 4.9: Measured susceptibility at 0V and 40V for the unsalted NaMt sample. At ≈ 55 ps for the 0V and ≈ 69 ps for 40V, there is a crossover point observed that differentiates the dynamic processes present on the system.

The primary outcome derived from the susceptibility plotting is the observation of two distinct dynamic processes in both the DIW and NaCl samples under both applied electric fields. These processes include a slower dynamic attributed to the narrow Lorentzians and a faster dynamic associated with the broad Lorentzians.

A logical progression would involve a direct comparison between the Q-subgroups containing salt and those without salt, as well as between the Q-subgroups with and without the application of an electric field. The most worth mentioning results arised from the first Q-subgroup at Q=0.4 $Å^{-1}$ and are shown in figure 4.10.

The left panel of the figure shows a direct comparison at Q=0.4 $Å^{-1}$ for the DIW NaMt sample at 0 and 40V. The impact of the electric field on the dynamics of water molecules in the system is evident, particularly regarding the faster dynamics. It is apparent that the application of an electric field induces a more pronounced and rapid change in these dynamics. Surprisingly, these results contradict what was obtained from the fitted QENS spectra which showed no EF effect on the samples. The right panel of the figure shows a direct comparison at 0V between the deionized and salted samples. Inconsistent with the QENS analysis, the fitting of the curves reveals that the inclusion of NaCl has a discernible impact on the dynamics. The rest Q-values in both cases did not show any worth mentioning results and can be found in appendix 6.3.

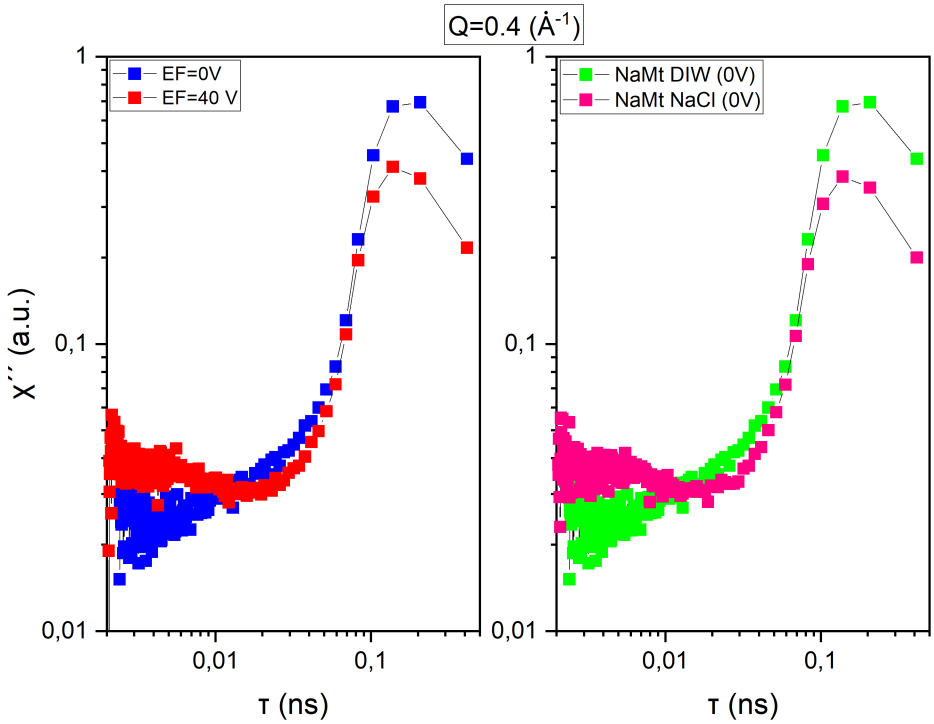

Figure 4.10: Comparison of susceptibility at Q=0.4 $Å^{-1}$. Left panel: Effect of EF on the DIW NaMt sample and right panel: Effect of NaCl on the NaMt samples.

The last step was to plot the EISF according to eq. 2.11 and the results are shown below at figure 4.11. In both samples and for both applied EFs, the same behavior is observed, with the data at EF=40V and 50V being slightly higher than those at EF=0V. The results of the fittings are shown in table 4.4. Fitting of the data with a less compatible model can be found in appendix 6.4.

Upon comparing the results with respect to changes in salinity or the applied electric field, no significant alterations are observed in the values of the immobile fraction p_{rc} or the radius of rotation a_{rc}. This suggests that the environment induced by the Na^+ cation remains unchanged in the presence of either the electric field or the addition of salt.

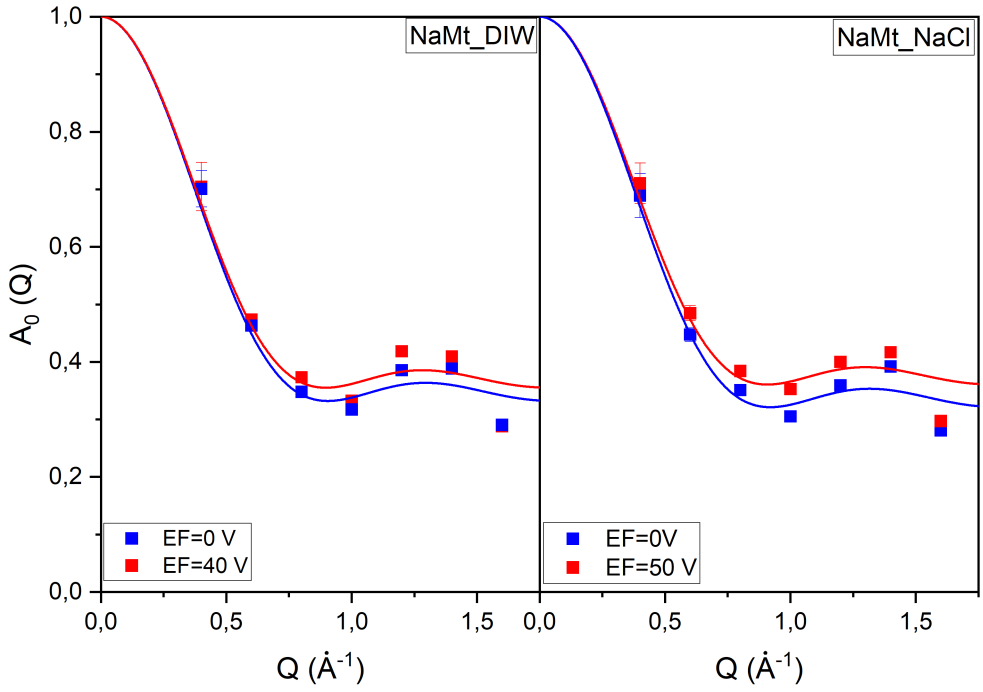

Figure 4.11: Fitted EISF according to eq. 2.11. In both kind of samples the EISF at 40V is slightly higher than the one at 0V. Both shown fits are having masked the data points were the Bragg reflections were observed.

Table 4.4: The radius of rotation, a_{rc}, and the immobile fraction of protons, p_{rc}, obtained from the fitting of the EISF with eq.2.11. None of the samples exhibited any discernible effects of the electric field or salinity, indicating that the environment surrounding the molecules remained unaltered despite variations in the experimental conditions of the samples.

Parameters	p_{rc} (%)	a_{rc} (Å)
NaMt *DIW* (0V)	0.35±0.02	3.50±0.39
NaMt *DIW* (40V)	0.33±0.02	3.47±0.30
NaMt *NaCl* (0V)	0.36±0.02	3.46±0.34
NaMt *NaCl* (50V)	0.32±0.02	3.42±0.31

4.2.2 Calcium Montmorillonite CaMt

The third sample that was studied was hydrated CaMt (figure 4.12). In this case the sample included 0.243 mL of 0.5M $CaCl_2$ (28.04 % GWC). The main purpose of the analysis of this sample is to see the effect that has the exchange of the cation in the smectite.

Figure 4.12: Prepared CaMt sample in its' sample holder.

In figure 4.13 the 7 Q-subgroups of the data are depicted. In this sample, we notice two Bragg reflections at Q=0.4 and 1.4 $Å^{-1}$, again due to the clay structure. In the inset figure the total fitting at Q=1 $Å^{-1}$ is shown. The fitting required again the use of a δ-function (green dashed line) as the resolution function, a linear background (purple solid line) and two Lorentzian functions (a narrow one: magenta dashed line and a broad one: orange dashed line).

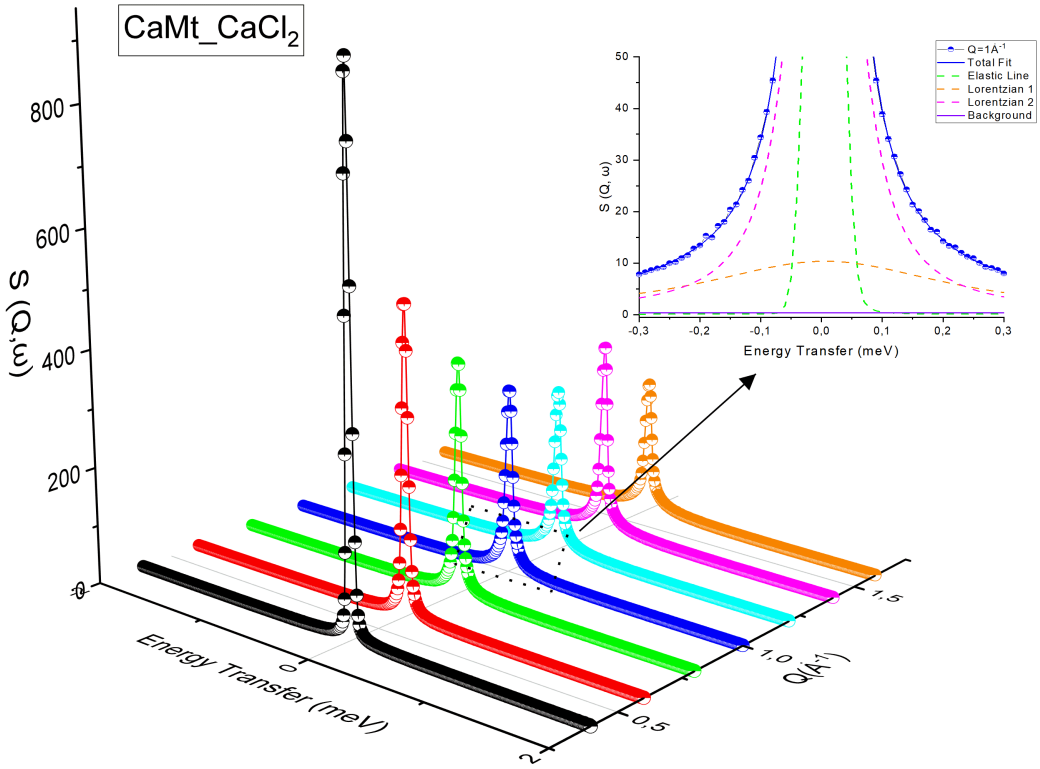

Figure 4.13: QENS spectra at EF=0 V for the CaMt sample for subgroups from 0.4 to 1.6 $Å^{-1}$ Q-values. Inset: Total fitting of the spectrum at Q=1 $Å^{-1}$ with a resolution function (green dashed line), 2 Lorentzian functions (narrow: magenta dashed line and broad: orange dashed line) and a linear background (purple solid line).

The exported HWHM from the fitted QENS spectra showed the dependence shown at figure 4.14. The fitting of the slower process (top panel of the figure) was once again done using the SSM, while the faster one (bottom panel of the figure) with the CEM. The Bragg reflection at Q=1.4 $Å^{-1}$ was not included in the fittings. The values of the D_t, as well as the τ are shown in table 4.5.

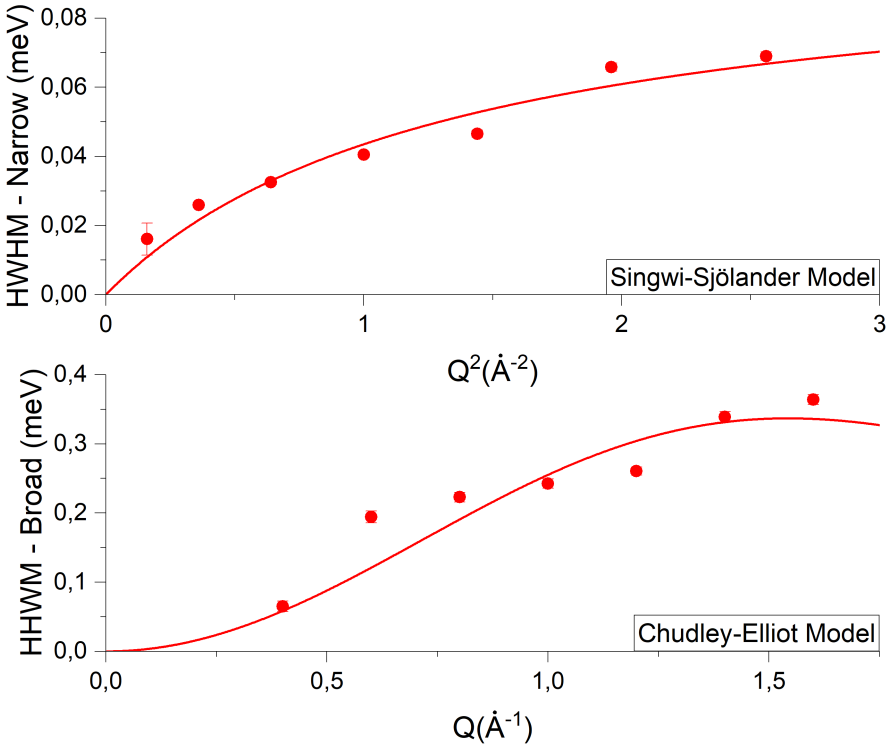

Figure 4.14: Q-dependence of the HWHM of the $CaCl_2$ sample of the narrow and broad lorentzian and their fitting with the SS and CE models respectively.

Table 4.5: Results for the diffusion coefficient for both narrow and broad Lorentzians at 0V for the CaMt sample. Comparing these results to the equivalent ones for the saline NaMt sample at EF=0V, the diffusion rate of the water molecules in the slower dynamic process remains unaffected, while the remaining parameters exhibit notably smaller magnitudes.

Parameters	Narrow Lorentzian	Broad Lorentzian
D_t (10^{-9} m^2/s)	1.2±0.2	- -±- -
τ (ps)	7.2±1.1	3.6±0.4
ℓ (Å)	2.28±0.04	2.9±0.4

In figure 4.15 the susceptibility for 3 Q-values is depicted. This parameter allowed us once again to confirm that there are indeed two dynamic processes detected. The crossover point in this sample is at $\approx$ 69 ps. The susceptibility for all Q-vectors can be found in appendix 6.2.

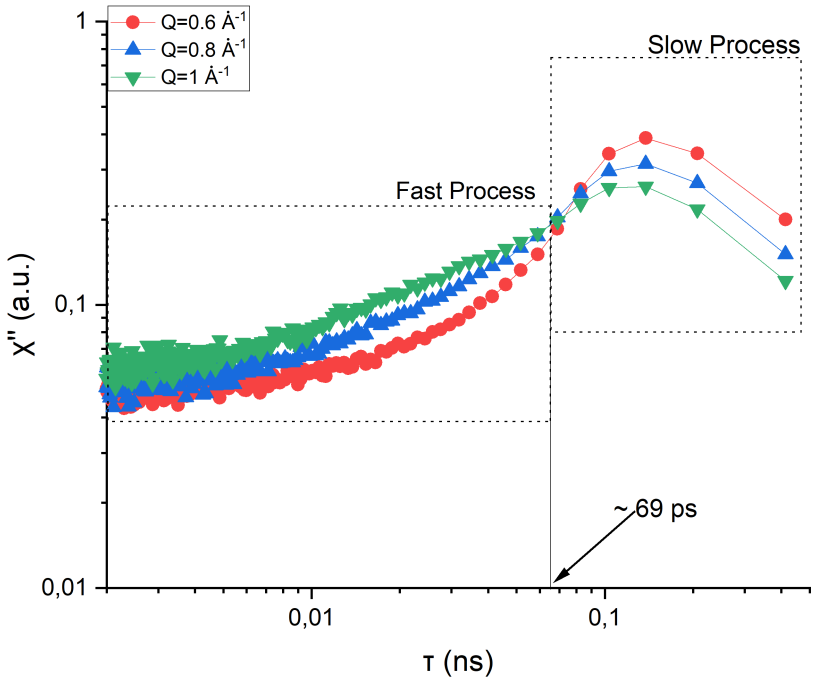

Figure 4.15: Susceptibility at EF=0V for the $CaCl_2$ CaMt oriented clay mineral film. The slower and faster dynamics are dissociated at ≈ 69ps.

Firstly, we can compare the values obtained for NaMt-NaCl at EF=0V with those for CaMt-$CaCl_2$ at EF=0V. What we observe is that the diffusion rate of the water molecules is comparable, while the residence time and the jump length are much lower in the CaMt sample in both dynamic processes. These values indicate that the environment the water molecules are in, is different in the presence of each cation. While both are about the same size, having ionic raddi ≈ 100 pm for Ca^{2+} and 95 pm for Na^{+}, their charge is different. Since Ca has a larger charge than Na, the bonds it can make with the water molecules are much stronger. Another case is that due to the cation's charge, Ca^{2+} might be more strongly attracted to the negatively charges surfaces of the clay mineral and is located nearer to one interlayer surface. This means that the cation is an important factor in distorting the hydrogen bonds.

Another thing to observe is the residence time regarding the slower process (narrow lorentzian). The τ value in this sample is comparable with the one found during Ignazzi's et al. studies [6] within the estimated errors, as well as previously reported values for a similar kind of sample. The lower value of ℓ indicates that the water molecules in the CaMt sample are much more

constrained and are not able to jump far from the initial position within a single jump. This has to do with the presence of $CaCl_2$ and the fact that in this case the water has to contend with both Ca and Cl and this disrupts its' ability to form H-bonds with other water molecules.

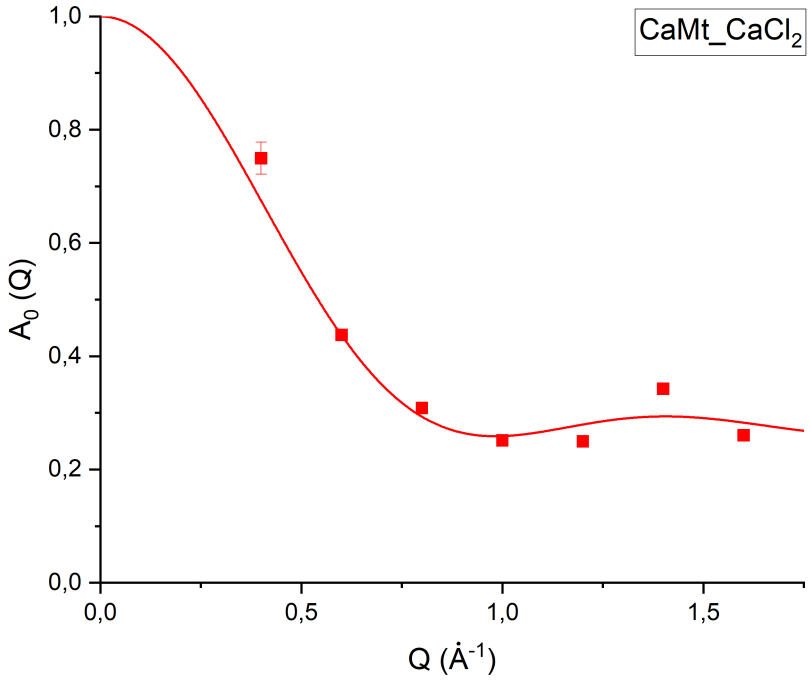

Figure 4.16: Fitted EISF for the $CaCl_2$ CaMt sample according to eq. 2.11.

In figure 4.16 the plotted and fitted EISF is depicted following eq.2.11. The derived parameters can be found in table 4.6. Regarding the immobile fraction of protons p_{rc}, it becomes apparent that in the CaMt sample, this fraction is considerably lower compared to the NaMt sample. This observation aligns with the notion that around a Ca^{2+} cation, a greater number of water molecules (6) would be expected compared to a Na^{+} cation (4). Fitting of the data with a less compatible model can be found in appendix 6.4.

Table 4.6: The radius of rotation, a_{rc}, and the immobile fraction of protons, p_{rc}, obtained from the fitting of the EISF with eq. 2.11.

Parameters	p_{rc} (%)	a_{rc} (Å)
CaMt $CaCl_2$	0.26±0.02	3.19±0.25

Last thing to compare is the susceptibility between the comparable samples of NaCl NaMt and $CaCl_2$ CaMt at EF=0V (figure 4.17). The figure displays two distinct behaviors, indicating significant differences between the samples. While both samples exhibit similar behavior during the slower dynamics, their trajectories diverge notably after their crossover points. More specifically, the CaMt sample (light blue curve) demonstrates a more linear behavior compared to the NaMt sample (black curve). Additionally, the signal intensity of CaMt is considerably higher than that of NaMt. These observations further support the notion that cations exert a significant influence on water diffusion by altering the surrounding environment.

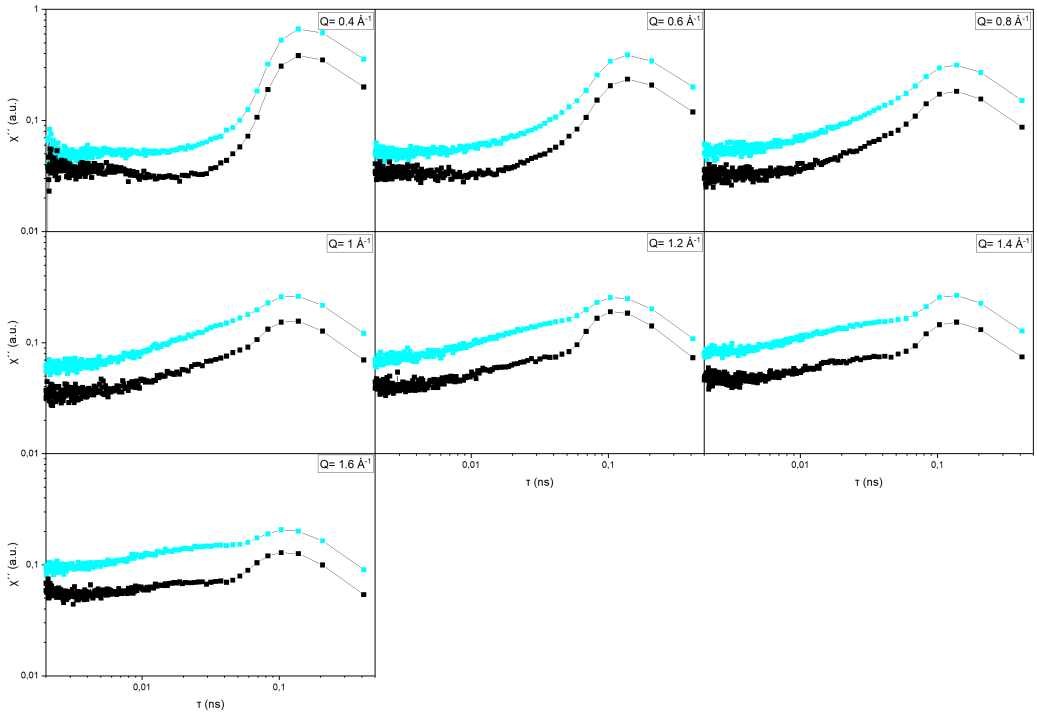

Figure 4.17: Comparison of the susceptibility between the NaCl NaMt and $CaCl_2$ CaMt samples at EF=0V. The distinct behavior of each sample underlines the impact of the type of the cation within the clay mineral interlayer.

5 Discussion and Perspectives

Regarding the bulk-water measurements the values obtained for the diffusion coefficient in the four different temperatures, $D_{t(280K)} \simeq 1.61\ 10^{-9}$ m^2/s, $D_{t(290K)} \simeq 2.07\ 10^{-9}$ m^2/s, $D_{t(300K)} \simeq 2.57\ 10^{-9}$ m^2/s and $D_{t(310K)} \simeq 3.08\ 10^{-9}$ m^2/s, are all in good agreement, both within the different methods and with the bibliography [10, 11, 12, 13, 14]. This indicated that all three methods used for the analysis are comparable and equally useful for the analysis of QENS set of data. It was also shown that the Singwi-Sjölander model, a jump diffusion model, is the one that best describes the dynamics of the bulk water molecules. The activation energies calculated from the obtained diffusion coefficients at different temperatures were found to be comparable across the different approaches used in this study. Furthermore, these calculated values align well with the existing literature on the subject [11]. Last thing to underline is that all studies on bulk-water, including this one, have been done in instruments with different resolutions, a fact that indicated that in the case of bulk-water there is indeed only one motion to be detected.

In relation to the NaMt samples, a study was conducted to investigate the influence of an electrical field and the inclusion of salt on the diffusion characteristics of water molecules confined within them. The instrument resolution allowed us to distinguish two separate motions present in the system; a slower population and a faster one. The slower population was interpreted with the SS jump diffusion model, while the faster one was done with the CE diffusion model. From the derived parameters, the conclusion was apparent that neither EF nor the presence of 0.5M NaCl affect the mobility of the water molecules in neither of the populations. Residence times and jump lengths are compa-

rable with each other within the error limitation which means that the water molecules' motions are weakly affected by external factors. The results of the residence times of the slower process indicated that the molecules spend a significant amount of time on each position before jumping to the next one, which is essentially far away from the initial position, while the oposite is true for the faster one. This should be an indication that the water population described by the fast process is more tightly bound within the clay system, either with the cation or with the interlayer surface (faster surface, slower cation). It might move fast, but the subsequent jumps are much more restricted in space.

The most interesting observation arised from the plotting of the susceptibility and especially at the lowest Q-value. As discussed above, the QENS analysis showed no respectful effects of the EF or the change of the salinity on the NaMt samples. At the same time, the susceptibility, except from confirming the existence of two separate dynamic processes in the system, it also revealed at Q=0.4 Å^{-1} that both EF and NaCl affected the diffusion of the water molecules confined within the clay mineral pores. At this furthest distance (d=$\frac{2\pi}{Q}$), there is all the information we can get for the sample, but at the same time we have the lowest QE signal, meaning that a need to further our studies arises, so as to focus not only on a better resolution, but also on this low Q-value.

Regarding the CaMt sample, the analysis showed that there are again two discrete dynamic processes, further confirmed by plotting the susceptibility. When comparing to the respective NaMt sample (0.5M NaCl NaMt at 0V), although the diffusion coefficients are comparable within the experimental errors, the residence time and jump length were significantly smaller in value for the slower motion. This result should have been anticipated, since different cations induce different environments for the water molecules and their different charges influence the water molecules' bonding either with the water molecules or with the clay surface, thus affecting the mobility in the interlayer. The fact, though, that for both dynamic processes the τ and ℓ values were so small, indicated that although the motions in the CaMt sample are more rapid, the molecules still stay within strong confinement.

Last result of the clay mineral oriented films to be referred is the EISF fittings. The best fitting model for our data appeared to be the isotropic rotation,

which gave us an insight into the mobile fraction of the protons within the water molecules. In the case of CaMt, a higher abundance of mobile protons was observed compared to NaMt, which aligns with the fact that Ca cations are surrounded by 6 water molecules while Na cations are surrounded by only 4. Further investigation of this phenomenon can be conducted using NMR spectroscopy, which can provide more detailed insights into the dynamics and interactions between cations and water molecules in the respective systems.

Future work to be done from a next student is mainly to work on the beidellite samples, as well as the effect of the orientation of the films on the results. The study of the orientation can actually give as information on whether the molecules have a preferred direction when they get polarized. After studying how the water molecules diffuse in the clay minerals, we can move on to some Thermoravimetric analysis and Infrared Spectroscopy. In this way we will get insight into the thermal stability of the samples, as well as some insight into the chemical composition.

Appendices

6

6.1 Units in the Singwi-Sjölander Model

In the Singwi-Sjölander model, the Q-dependence of the Lorentzian half-widths, Γ, is given by:

$$\Gamma(Q) = \frac{\hbar D_t Q^2}{1 + D_t \tau_0 Q^2} \tag{6.1}$$

where Γ is in units of meV and the momentum transfer, Q, is in units of Å^{-1}. In order to have the diffusion coefficient, D_t, in untis of $10^{-9} m^2/\text{s}$ and the relaxation time τ_0 in units of ps, a conversion factor is needed in the numerator and the denominator as well as a proper choice of units for $\hbar$.
For $\hbar$ we choose units of meVs, $\hbar$=6.582 10^{-13} meVs and since Q is in units of Å^{-1} we have:

$$Q^2 = (\text{Å}^{-1})^2 = (10^{-10})^{-2} = 10^{20} m^{-2} \tag{6.2}$$

Considering first the denominator, we notice that $D_t\ \tau_0\ Q^2$ must be dimensionless and inserting the desired units for D_t and τ_0 we get:

$$D_t \tau_0 Q^2 = (10^{-9} m^2 s^{-1})(10^{-12} s)(10^{20} m^{-2}) = 0.1 \tag{6.3}$$

which is the required conversion factor.
For the numerator we get:

$$\hbar D_t Q^2 = (6.58210^{-23} meV s)(10^{-9} m^2 s^{-1})(10^{20} m^{-2}) = 0.06582 meV \tag{6.4}$$

which is the required conversion factor for a Lorentzian half-width in units of meV. As a result, the Singwi-Sjölander model in the desired units is:

$$\Gamma(Q) = \frac{0.06582 D_t Q^2}{1 + 0.1 D_t \tau_0 Q^2} \tag{6.5}$$

6.2 Susceptibility Plotting

This section includes the calculated susceptibility for all Q-subgroups.
In figure 6.1 the susceptibility for the DIW NaMt sample is depicted for 0V (left panel) and 40V (right panel) applied EF.

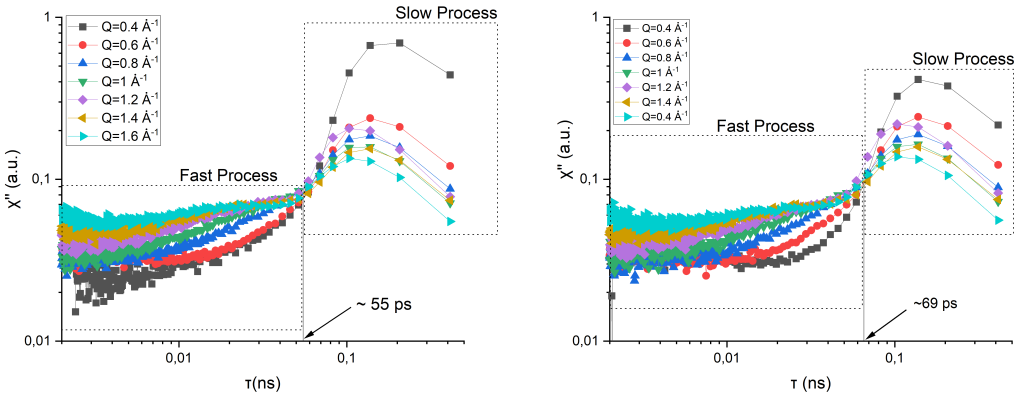

(a) Susceptibility of DIW NaMt at 0V. **(b)** Susceptibility of DIW NaMt at 40V.

Figure 6.1: Measured susceptibility at 0V an 40V for the unsalted NaMt sample including all Q-subgroups.

In figure 6.2 the susceptibility for the 0.5M NaCl NaMt sample is depicted for 0V (left panel) and 50V (right panel) applied EF.

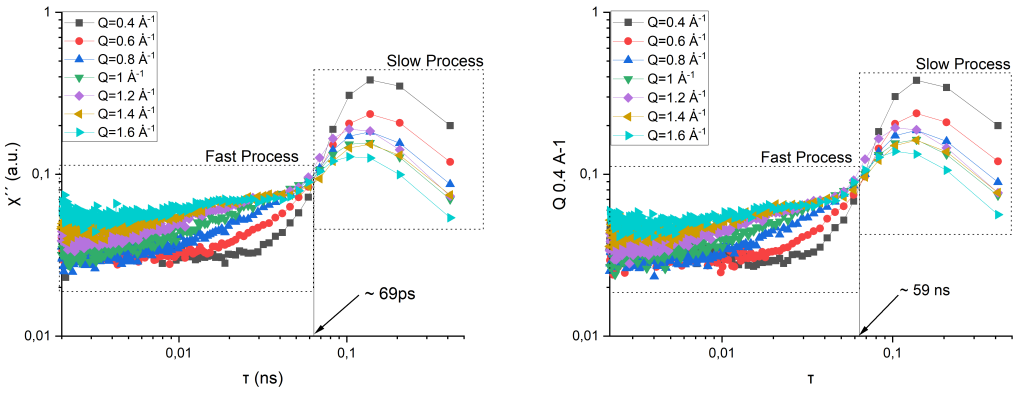

(a) Susceptibility of 0.5M NaCl NaMt at 0V. **(b)** Susceptibility of 0.5M NaCl NaMt at 50V.

Figure 6.2: Measured susceptibility at 0V an 40V for the 0.5M NaCl NaMt sample including all Q-subgroups.

In figure 6.3 the susceptibility for the 0.5M $CaCl_2$ CaMt sample is depicted for 0V applied EF.

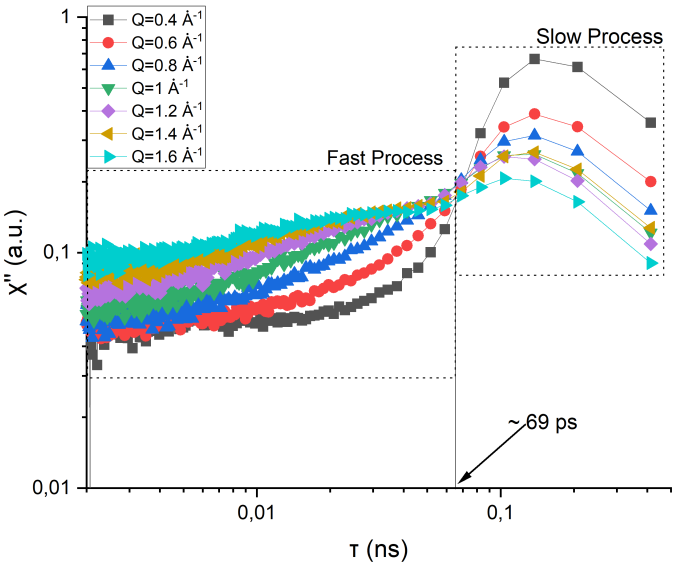

Figure 6.3: Measured susceptibility for the 0.5M $CaCl_2$ sample including all Q-subgroups.

6.3 Susceptibility Comparisons

Figure 6.4 shows the effect of EF on the deionized NaMt sample at the rest of the Q-subgroups from 0.6 to 1.6 Å^{-1}. From the figures the conclusion can be drawn that no direct effect is observed on these Q-values contradicting what was shown for Q=0.4 Å^{-1}.

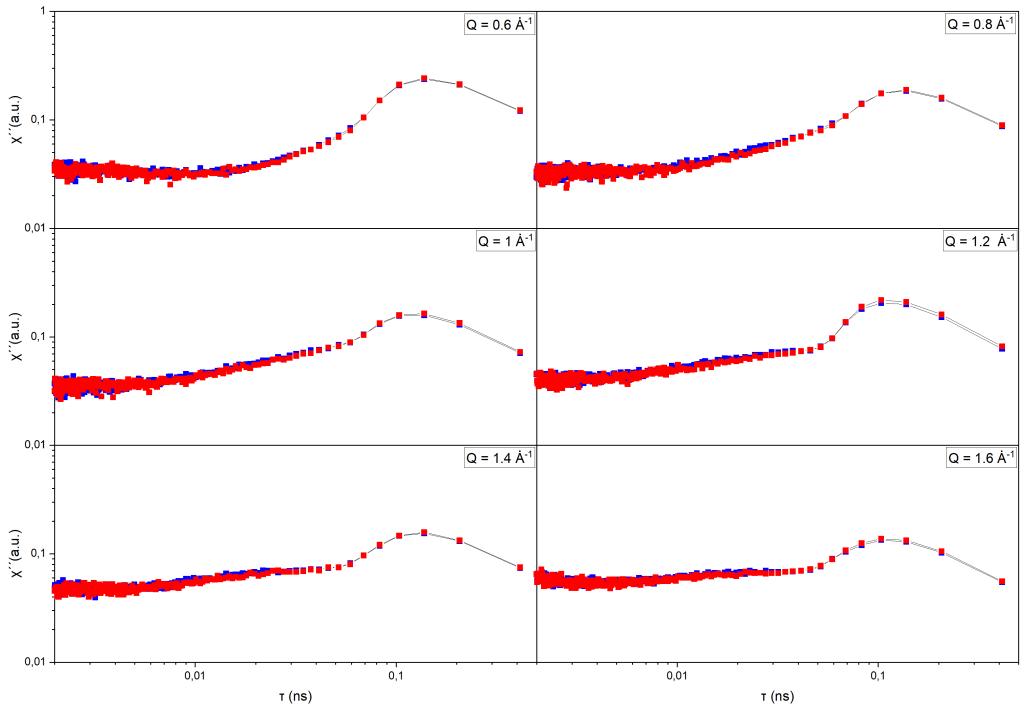

Figure 6.4: Effect of EF application on the DIW NaMt sample at Q-subgroups: Q=0.6 Å^{-1} to 1.6 Å^{-1}.

Figure 6.5 shows the effect of EF on the 0.5M NaCl NaMt sample at the Q-subgroups 0.4 to 1.6 Å^{-1}. Although there is an indication of slight effects of the EF when the sample contained salt, the instrumental resolution does not allow us to draw any strict conclusions even from the lowest Q-vector.

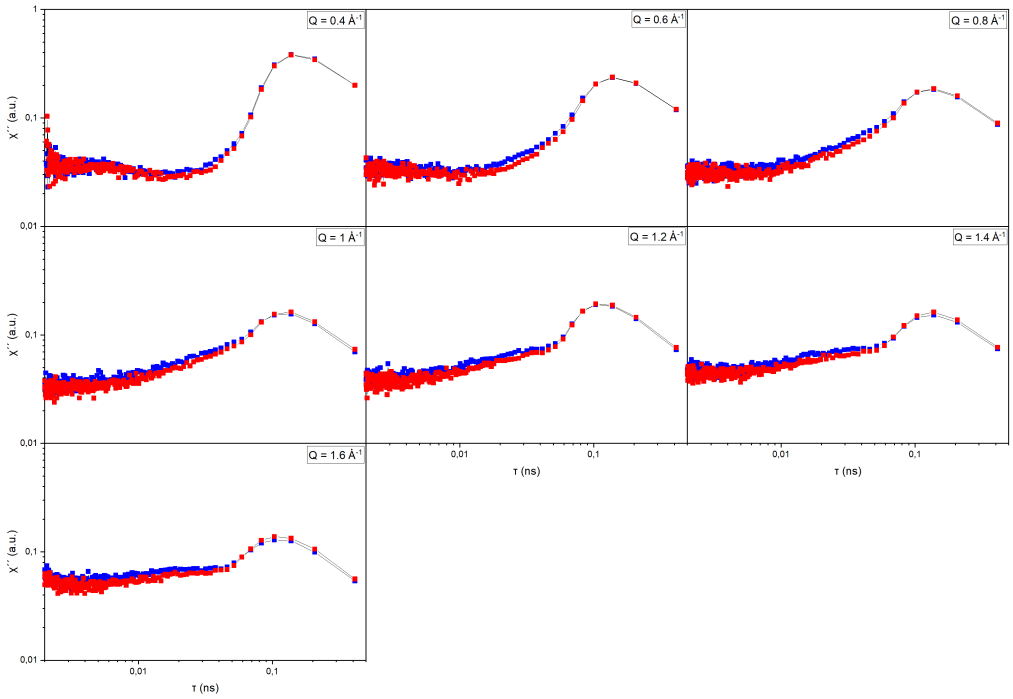

Figure 6.5: Effect of EF application on the 0.5M NaCl NaMt sample at Q-subgroups: Q=0.4 Å^{-1} to 1.6 Å^{-1}.

Figure 6.6 shows the effect of NaCl on the NaMt samples at the rest of the Q-subgroups from 0.6 to 1.6 Å^{-1} when EF=0V. From the figures it can be inferred that no direct effect is observed on these Q-values in contrast to what was shown for Q=0.4 Å^{-1}.

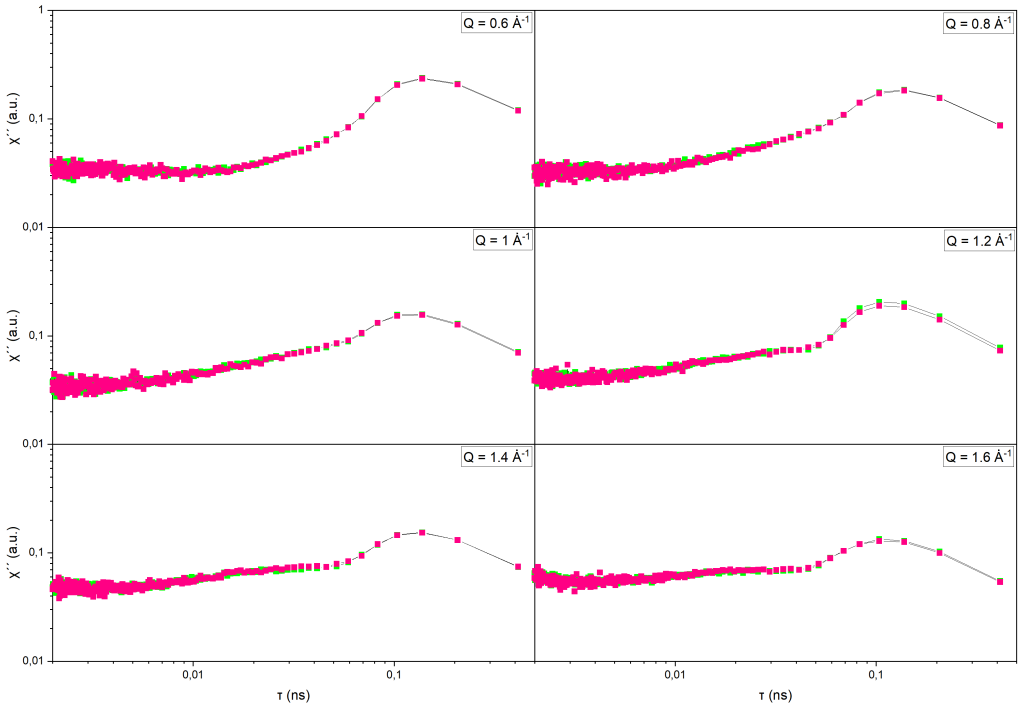

Figure 6.6: Effect of salinity concentrations changes on the NaMt samples at EF=0V at Q-subgroups: Q=0.6 Å^{-1} to 1.6 Å^{-1}.

Figure 6.7 shows the effect of NaCl on the NaMt samples at the Q-subgroups 0.4 to 1.6 Å^{-1} when EF is applied. From this evidence there is only a slight effect observed on these Q-values which might as well come from the fact that the salted sample was probed in a higher applied EF than the DIW sample(50V instead of 40V).

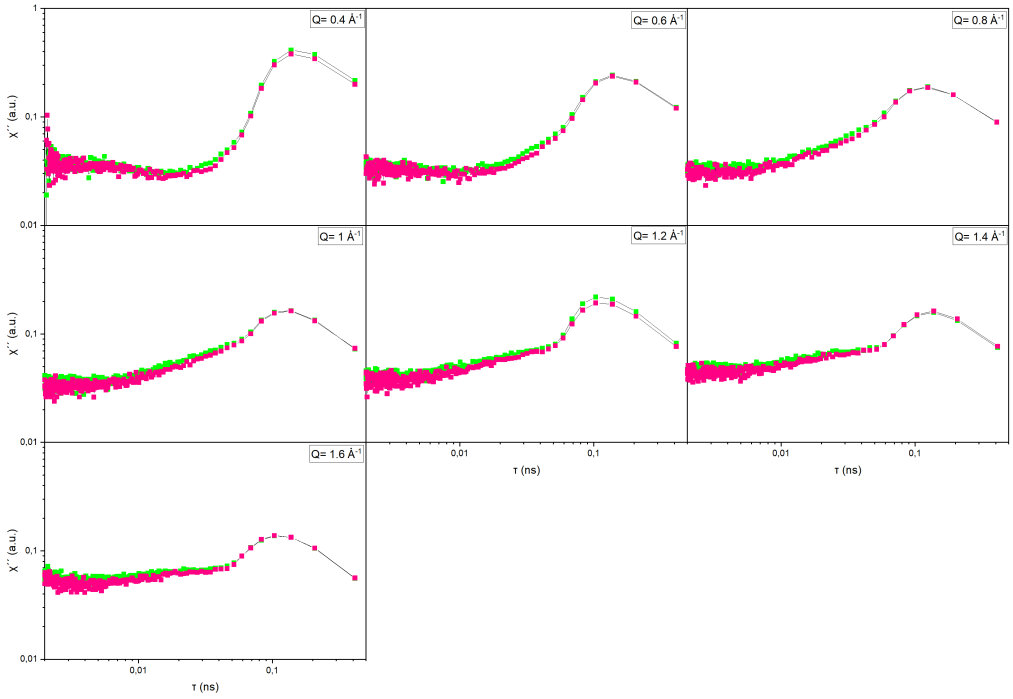

Figure 6.7: Effect of salinity concentrations changes on the NaMt samples at applied EF at Q-subgroups: Q=0.4 Å^{-1} to 1.6 Å^{-1}.

6.4 EISF fittings

As stated in the main body of this thesis, the fitting of the EISF was done using different methods, which seemingly did not yield precise data fitting. Among these models one approach refers to an effective EISF that offers insight into the collective dynamics of all motions captured within the observation timeframe of the spectrometer. The following equation [37]:

$$EISF = A_0(Q) = p + (1-p) \times \left[\frac{3}{Qr}\left[\frac{sin(Qr)}{(Qr)^2} - \frac{cos(Qr)}{(Qr)}\right]\right]^2 \tag{6.6}$$

where r is the radius of the idealized spherical confinement and p accounts for the immobile fraction of the protons is commonly used to analyze water in confinement. The fittings are shown in figure 6.8 and the fitted parameters in table 6.1. The same fitting was done for the 0.5M $CaCl_2$ CaMt sample as well.

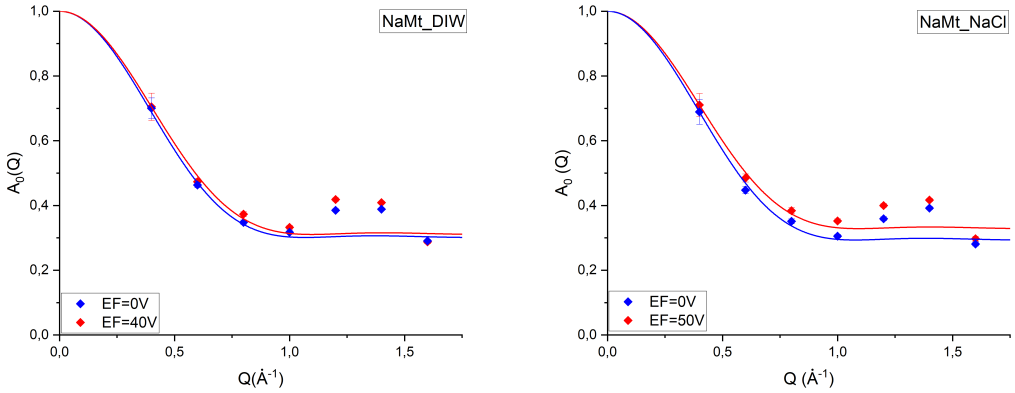

(a) EISF fit of DIW NaMt.

(b) EISF fit of 0.5M NaCl NaMt.

Figure 6.8: Fitting of the NaMt samples using the modified EISF model representing confinement.

Table 6.1: The radius of confinement, r, and the immobile fraction of protons, p, obtained from the fitting of the EISF with eq.6.6. All values seem comparable within the experimental errors.

Parameters	p (%)	r (Å)
NaMt *DIW* (0V)	0.37±0.02	4.64±0.79
NaMt *DIW* (40V)	0.35±0.02	4.59±0.62
NaMt *NaCl* (0V)	0.37±0.02	4.57±0.69
NaMt *NaCl* (50V)	0.34±0.02	4.56±0.65

The plot can be found in figure 6.9 and the fitting results in table 6.2.

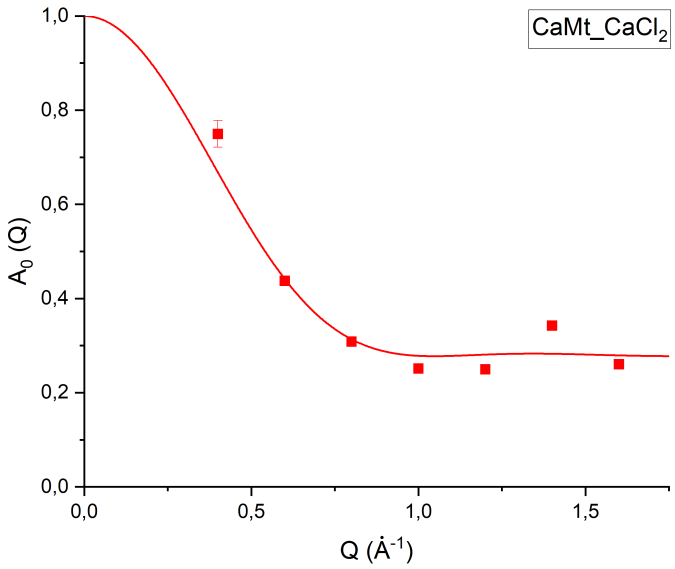

Figure 6.9: Fitting of the CaMt sample using the modified EISF model representing confinement.

Table 6.2: The radius of confinement, r, and the immobile fraction of protons, p, obtained from the fitting of the EISF with eq.6.6.

Parameters	p (%)	r (Å)
CaMt $CaCl_2$	0.28±0.02	4.28±0.55

Despite the ineffectiveness of the fitting with this model in all three samples, as evidenced by the exclusion of somr values from the fitting curve, a comparison of the p-values suggests a higher degree of mobility in the CaMt sample compared to the NaMt sample.

Bibliography

[1] J. Teixeira *et al.* „Experimental determination of the nature of diffusive motions of water molecules at low temperatures“. In: *Physical Review A* 31 (1985), p. 3.

[2] Patrice Porion *et al.* „Water and Ion Dynamics in Confined Media: A Multi-Scale Study of the Clay/Water Interface“. In: *Colloids and Interfaces* 5 (2021), p. 34.

[3] W. P. Gates *et al.* „Layer charge effects on anisotropy of interlayer water and structural OH dynamics in clay minerals probed by high-resolution neutron spectroscopy“. In: *Applied Clay Science* 201 (2021), p. 105928.

[4] Heloisa Bordallo *et al.* „Quasi-Elastic Neutron Scattering Studies on Clay Interlayer-Space Highlighting the Effect of the Cation in Confined Water Dynamics“. In: *J. Phys. Chem. C.* 112 (2008), pp. 13982–13991.

[5] M. L. Martins *et al.* „Neutron Scattering, a powerful tool to study clay minerals“. In: *Applied Clay Science* 96 (2014), pp. 22–35.

[6] Rosanna Ignazzi *et al.* „Electric Field Induced Polarization Effects Measured by in Situ Neutron Spectroscopy“. In: *J. Phys. Chem. C* 121 (2017), pp. 23582–23591.

[7] „Ajka alumina plant accident“. In: *Wikipedia: https://en.wikipedia.org/wiki/Ajka_alumina_plant_accident* ().

[8] O. Arnold *et al.* „Mantid-Data analysis and visualization package for neutron scattering and μ SR experiments“. In: *Nuclear Instrument and Methods in Physics Research A* 764 (2014), pp. 156–166.

[9] Martin H. Petersen *et al.* „Assessing Diffusion Relaxation of Interlayer Water in Clay Minerals Using a Minimalist Three-Parameter Model“. In: *J. Phys. Chem. C.* 125 (2021), pp. 15085–15093.

[10] Sow *et al.* „Incoherent quasielastic neutron scattering from water in supercooled regime“. In: *Physical Review A.* 26 (1982).

[11] R. Mills. „Self-Diffusion in Normal and Heavy Water in the Range 1-45°“. In: *The Journal of Physical Chemistry* 77 (1973), p. 5.

[12] William Price *et al.* „Self-Diffusion of Supercooled Water to 238 K Using PGSE NMR Diffusion Measurements“. In: *J. Phys. Chem. A.* 103 (1999), pp. 448–450.

[13] Manfred Holz *et al.* „Temperature-dependent self-diffusion coefficients of water and six selected molecular liquids for calibration in accurate 1H NMRPFG measurements“. In: *Phys. Chem. Chem. Phys.* 2 (2000), pp. 4740–4742.

[14] P.S. Tofts *et al.* „Test Liquids for Quantitative MRI Measurementsof Self-Diffusion Coefficient In Vivo“. In: *Magnetic Resonance in Medicine* 43 (2000), pp. 368–374.

[15] R.T. Azuah *et al.* „DAVE: A comprehensive software suite for the reduction, visualization, and analysis of low energy neutron spectroscopic data“. In: *J. Res. Natl. Inst. Stan. Technol. 114* 341 (2009).

[16] Zhou *et al.* „Nanomaterials from Clay Minerals“. In: *Micro and Nanotechnologies* (2019), pp. 335–364.

[17] Q. Berrod *et al.* „Inelastic and quasi-elastic neutron scattering. Application to soft matter“. In: *EBJ Web of Conferences* 188 (2018), p. 05001.

[18] Kim Lefmann. „Neutron scattering: Theory, instrumentation and simulation.“ In: *Notes from the course "Neutron scattering"* (2022).

[19] Marcella C. Berg. „Dynamics of liquids confined in porous materials: A quasi-elastic study.“ In: *Ph.D Thesis, X-Ray and Neutron Science* (2017).

[20] T.Gutberlet J.Fitter and J.Katsaras. „Neutron Scattering in Biology: Techniques and applications“. In: *Biological and Medical Physics / Biomedical Engineering* (2006), pp. 321–322.

[21] Andrew T. Boothroyd. „Principles of Neutron Scattering from Condensed Matter“. In: *Oxford University Press* (2020).

[22] J.Jacobsen *et al.* „Nano-scale hydrogen-bond network improves the durability of greener cements“. In: *Scientific Reports* 3 (2013), p. 2667.

[23] M. Bee. „A physical insight into the elastic incoherent structure factor“. In: *Physica B: Condensed Matter* 182 (1992), pp. 323–336.

[24] M. Bee. „Quasielastic neutron scattering : principles and applications in solid state chemistry, biology, and materials science“. In: *Bristol* England (1988), Adam Hilger.

[25] C. T. Chudley and R. J. Elliott. „Neutron Scattering from a Liquid on a Jump Diffusion Model“. In: *Proc. Phys. Soc.* 77 (1961), p. 353.

[26] J. Peters M. Saouessi and G. R. Kneller. „Asymptotic analysis of quasielastic neutron scattering data from human acetylcholinesterase reveals subtle dynamical changes upon ligand binding“. In: *J. Chem. Phys.* 150 (2019), p. 161104.

[27] Gerald R. Kneller. „Frank-Condon picture of incoherent neutron scattering“. In: *PNAS* 115 (2018), pp. 9450–9455.

[28] J. Peters M. Saouessi and G. R. Kneller. „Frequency domain modeling of quasielastic neutron scattering from hydrated protein powders: Application to free and inhibited human acetylcholinesterase“. In: *J. Chem. Phys.* 151 (2019), p. 125103.

[29] Martin H. Petersen *et al.* „Revisiting the modeling of quasielastic neutron scattering from bulk water“. In: *EPJ Web of Conferences* 272 (2022), p. 01012.

[30] „Iris“. In: *ISIS official website: https://www.isis.stfc.ac.uk/Pages/iris.aspx* ().

[31] K. Nakajima *et al.* „Recent Update of AMATERAS: a Cold-Neutron Disk-Chopper Spectrometer“. In: *JPS Conf. Proc.* 33 (2021), p. 011089.

[32] K. Nakajima *et al.* „Amateras: A cold-neutron disk chopper spectrometer“. In: *Journal of the Physical Society of Japan* 80:SB028 (2011).

[33] Martin H. Petersen. „Molecular Dynamic Analysis of Quasi-Elastic Neutron Scattering from Bulk and Confined Water“. In: *MSc Thesis, Niels Bohr Institute* (2022).

[34] Yasuhiro Inamura *et al.* „Development Status of Software “Utsusemi” for Chopper Spectrometers at MLF, J-PARC“. In: *J. Phys. Soc. Jpn.* 82 (2013).

[35] R Dimeo and L. Kneller. „Peak Analysis: PAN. A general-purpose curve=fitting program in DAVE“. In: (2002).

[36] J. J. Fripiat, M. Letellier, and P. Levite. „Interaction of water with clay surfaces“. In: *Phil. Trans. R. Soc. Lond. A* 311 (1984), pp. 287–299.

[37] Marcella C. Berg *et al.* „Nanoscale Mobility of Aqueous Polyacrylic Acid in Dental Restorative Cements“. In: *ACS Appl. Mater. Interfaces* 10 (2018), pp. 9904–9915.